

Available online at www.sciencedirect.com

ScienceDirect





Research Article

Penetrative biomimetic nanovehicle boosts immunotherapy in triple-negative breast cancer via SOS1 blockade



Jiaxin Zhang^{a,b}, Peng Xian^a, Chao Wang^c, Xier Pan^a, Yaoyao Du^a, Yunrong Nan^d, Qing Pu^a, Linghui Zou^a, Donovan Green^e, Shuting Ni^{f,*}, Kaili Hu^{a,*}

- ^a School of Pharmacy, Shanghai University of Traditional Chinese Medicine, Shanghai 201203, China
- ^b Department of Pharmacy, Huashan Hospital, Fudan University, Shanghai 200040, China
- ^cDepartment of Gynecology, Obstetrics and Gynecology Hospital of Fudan University, Shanghai 201203, China
- ^d Shanghai Innovation Center of TCM Health Service, Shanghai University of Traditional Chinese Medicine, Shanghai 201203, China
- ^e Chemical and Pharmaceutical Sciences, School of Human Sciences, London Metropolitan University, London N7 8DB, UK
- ^f Shanghai Frontiers Science Center of TCM Chemical Biology, Institute of Interdisciplinary Integrative Medicine Research, Shanghai University of Traditional Chinese Medicine, Shanghai 201203, China

ARTICLE INFO

Article history:
Received 4 November 2024
Revised 22 March 2025
Accepted 11 April 2025
Available online 2 May 2025

Keywords:
Son of sevenless 1
Triple-negative breast cancer
Tetrandrine
Docetaxel
Cilengitide
Liposome

ABSTRACT

Immunotherapy of triple-negative breast cancer (TNBC) is significantly hindered by the immunosuppressive tumor microenvironment (TME). Notably, tumor-associated macrophages (TAMs), which constitute the predominant infiltrating immune cell type in TNBC, represent a critical target for "turning off" immunosuppressive TME. Despite numerous ongoing clinical trials, current strategies exhibit limited efficacy in overcoming immunosuppressive TME. Interestingly, regulation of son of sevenless 1 (SOS1), which is overexpressed in TNBC patients, shows promising potential for TAM repolarization. Herein, we developed a biomimetic liposomal platform (CCM/Cil-lipo@TD), which integrates cilengitide (Cil)-functionalized breast cancer cell membranes (CCM) to co-deliver tetrandrine (TET) and low-dose docetaxel (DTX) for TNBC therapy. This system synergistically enhanced immunotherapy by coupling SOS1 blockade-driven TAM repolarization with immune cell death (ICD)-mediated dendritic cell (DC) maturation, thereby reshaping the highly immunosuppressive TME in TNBC. Critically, the low-density Cil-anchored, CCM-fused liposomes overcome the penetration limitations inherent to conventional CCM-based delivery systems, achieving deep intratumoral accumulation of therapeutic payloads. Mechanistically, the CCM/Cil-lipo@TD ensured that TET-mediated SOS1 inhibition in tumor cells efficiently polarized TAM2 (protumor) toward TAM1 (antitumor). Furthermore, SOS1 blockade synergized with low-dose DTX-induced ICD to remodel TME, as evidenced by sustained cytotoxic T-cell infiltration and suppression of regulatory T cells. The CCM/Cil-lipo@TD exerted superior tumor inhibition (82.9 %) in

E-mail addresses: stella_ni2021@163.com (S. Ni), kaili-hu@163.com (K. Hu). Peer review under responsibility of Shenyang Pharmaceutical University.

^{*} Corresponding authors.

4T1 orthotopic models and effectively inhibited postoperative local recurrence and distant metastasis. Taken together, the Cil-engineered, cell membrane-anchoring CCM/Cil-lipo@TD provides a promising approach for TNBC immunotherapy.

© 2025 Shenyang Pharmaceutical University. Published by Elsevier B.V.

This is an open access article under the CC BY-NC-ND license

(http://creativecommons.org/licenses/by-nc-nd/4.0/)

1. Introduction

Triple-negative breast cancer (TNBC), a highly invasive breast cancer subtype, is characterized by rapid progression and elevated recurrence risk [1,2]. Over 50 % of patients experience relapse within the first 3 to 5 years post-diagnosis [3,4]. Immunotherapy has recently emerged as a standard-of-care approach for TNBC [5]; however, immune-checkpoint inhibitor (ICI) monotherapy exhibits primary immune resistance. Consequently, combinatorial strategies with chemotherapy are required to overcome resistance and improve durable responses [5]. For instance, the KEYNOTE-522 trial indicated that combining ICIs with chemotherapy enhanced antitumor activity and reduced the distant recurrence risk by 39 % [5,6]. Nevertheless, clinical data reveals limited clinical benefits of ICI monotherapy in TNBC patients possibly due to the immunosuppressive tumor microenvironment (TME) [7]. Immune checkpoint blockades (ICBs) explicitly target the TME rather than the tumor cells themselves. ICB may be more effective in patients with immune-enriched tumors, which are characterized by high tumor-infiltrating lymphocytes (TILs) and immune checkpoint expression [8]. Tumor-associated macrophages (TAMs) constitute the major population of tumor-infiltrating leukocytes in breast tumors and drive immunosuppressive TME dynamics [9]. Several clinical trials involving TAM recruitment and accumulation (e.g., chemokines, CSF1, and signal transducer and activator of transcription 3), macrophage activation (e.g., CD40, toll-like receptors and STING), myeloid checkpoint inhibition (e.g., signal regulatory protein- α , CD47, scavenger receptors, and PD1), and adoptive macrophage therapy are ongoing [10,11]; however, the current strategies are not sufficient to overcome the immunosuppressive TME in TNBC [12]. Moreover, nonspecific monocyte/macrophage depletion will cause the loss of tissue-resident macrophages, whereas withdrawal of recruitment inhibition may accelerate metastasis [13]. Therefore, it is imperative to seek more precise biomarkers for reprogramming TAM in TNBC.

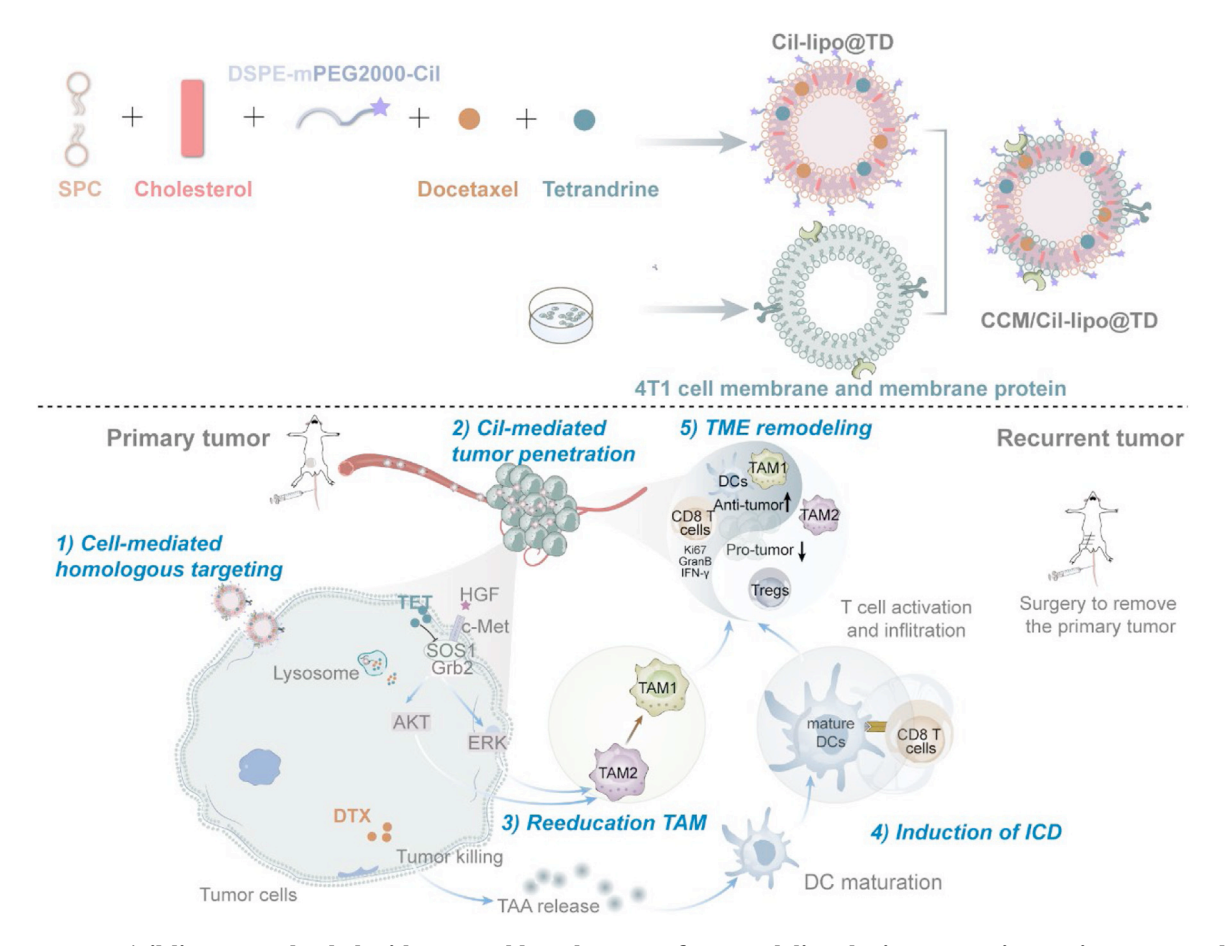
SOS1 is the major rat sarcoma-guanine nucleotide exchange factor (RAS-GEF) and triggers GTP loading toward the RAS (on) state. Consequently, mutationally activated RAS transmits environmental signals into the RAS-extracellular signal-regulated kinase (ERK) mitogen-activated protein kinase (MAPK) signaling and the phosphatidylinositol 3-kinase (PI3K)-protein kinase B (Akt)-mammalian target of rapamycin (mTOR) pathway [14]. Notably, SOS1 knockdown significantly inhibited lung metastasis of E0771 cells (mammary adenocarcinoma) [15], highlighting its potential as a therapeutic target for lung metastasis of TNBC patients. Furthermore, SOS1 knockdown significantly reduced M2

macrophage infiltration in breast cancer lung metastasis models [15], suggesting that SOS1 enhances the M1–M2 transition of macrophages. Taken together, these findings establish SOS1 overexpression in TNBC as a key regulator of TAM polarization. Therefore, the strategy we have adopted is to selectively regulate macrophage polarization by targeted inhibition of SOS1 on tumor cells.

Surgical adjuvant chemotherapy remains the major clinical treatment option for TNBC [3]. In addition, an increasing number of reports have suggested that certain chemotherapeutic drugs (e.g., doxorubicin, paclitaxel and docetaxel) can induce immunogenic cell death (ICD) [16,17]. The ICD of dying tumor cells is another promising strategy to elicit antitumor immunity [18]. Importantly, low-dose chemotherapy regimens have been shown to elicit antitumor immune responses while minimizing the systemic toxicity associated with conventional high-dose regimens [19]. Hence, leveraging low-dose chemotherapy to induce ICD may synergize with TAM repolarization-mediated strategies, offering a dual mechanism to strengthen antitumor immune responses and reshape the TME.

In this study, we propose a dual immune stimulation strategy involving simultaneous TAM repolarization and ICD induction by targeted codelivery of tetrandrine (TET) and low-dose docetaxel (DTX). TET is a bisbenzylisoquinoline alkaloid extracted from the root of the traditional Chinese medicine Stephania tetrandra S. Moore [20]. Attractively, TET is capable of inhibiting SOS1 expression [21] and demonstrates anti-TNBC activity [22]. Critically, SOS1 inhibition by TET is postulated to reprogram immunosuppressive TAM2 toward an antitumoral TAM1. Concurrently, DTX is a first-line chemotherapeutic agent approved for TNBC treatment. It has been reported that DTX can induce ICD in breast cancer cells for chemoimmunotherapy [17]. It is thus hypothesized that the synergistic effects of TET and low-dose DTX can amplify the anti-TNBC effect by relieving the suppressive TMF

To address the issue of targeted codelivery, we developed cancer cell membrane (CCM)-fused liposomes for codelivery of TET and DTX, simultaneously modified them with cilengitide (Cil), forming CCM/Cil-lipo@TD. CCM coating has attracted significant attention for anticancer drug delivery due to the self-target of cancer cells [23], prolonged systemic circulation, and enhanced cellular internalization [24]. Breast CCM-fused liposomes are expected to obtain membrane protein-mediated homologous targeting, thereby achieving specific drug delivery to tumor sites. Although CCM-fused liposomes have been widely studied, our study uniquely addresses the insufficient penetration of current tumor cell membrane-based therapies, enabling effective deep intratumoral delivery of TET and low-



Scheme 1 – CGM/Cil-lipo@TD coloaded with TET and low-dose DTX for remodeling the immune microenvironment and improving the therapeutic effect of TNBC. (1) Fused CGMs in CGM/Cil-lipo@DiD were designed to improve tumor accumulation by homologous targeting. (2) Low-density Cil modification enhanced tumor penetration via tumor vascular promotion. (3) CGM/Cil-lipo@TD effectively inhibited SOS1 expression and inactivated Akt and ERK signaling, thereby promoting TAM reprogramming. (4) CGM/Cil-lipo@TD could trigger the ICD of tumor cells and then induce DC maturation. (5) The CGM/Cil-lipo@TD potentiated effective antitumor immune responses via TAM repolarization and DC maturation, thus exerting superior tumor inhibition in 4T1 orthotopic models, and inhibiting both local recurrence and distant metastasis after surgical tumor resection.

dose DTX. More importantly, nanomolar-concentration Cil modification endowed these liposomes with the ability of deep intratumoral drug delivery [25]. Collectively, the low-density Cil-anchored CCM-fused liposomes exhibit excellent permeation-promoting activity compared to conventional CCM-coated systems, offering dual advantages of tumor specificity and deep intratumoral accumulation. Together with TET-mediated SOS1 inhibition and DTX-induced ICD, we anticipate that the CCM/Cil-lipo@TD would offer promising avenues for the anti-TNBC immunotherapy strategy through enhanced antitumor immune response (Scheme 1).

2. Materials and methods

2.1. Materials

TET was obtained from Chengdu Herbpurify Co., Ltd. (Chengdu, China). DTX was purchased from

South pharmaceutical Co., Ltd. (Fujian, China). Soy lecithin, cholesterol 1,2-distearoyl-sn-glyceroand 3-phosphoethanolamine-N-methoxyPEG2000 mPEG2000) were purchased from A.V.T. Pharmaceutical Co., Ltd. (Shanghai, China). Cil was obtained from Nanjing Leon Biological Technology Co., Ltd. (Nanjing, China). DSPEmPEG2000-NH2 was obtained from Xi'an Ruixi Biological Technology Co., Ltd. (Xi'an, China). Trizol RNAisoplus was obtained from Takara Biomedical Technology Co., Ltd. (Beijing, China). cDNA reverse transcription kit and PE conjugated Granzyme B were purchased from ThermoFisher Scientific (USA). Hieff® qPCR SYBR green master mix, fetal bovine serum (FBS), DiD, DiR, DiI, reactive oxygen species (ROS) assay kit, collagenase IV, and hyaluronidase were purchased from Yeasen Biotech Co., Ltd. (Shanghai, China). LumiQ enhanced chemiluminescence (ECL) reagent was purchased from Share-Bio Co., Ltd. (Shanghai, China). All qPCR primers (Table S1) were synthesized by Sangon Biotech Co., Ltd. (Shanghai, China). Phospho-p44/42 MAPK (Erk1/2) (Thr202/Tyr204) antibody, p44/42 MAPK (Erk1/2) antibody, BclxL, and phospho-Akt (Ser473) antibody were purchased from Cell Signaling Technology (USA). SOS1 antibody, calreticulin (CRT) antibody, and CD31 antibody were obtained from HuaBio Co., Ltd. (Hangzhou, China). HGF protein, recombinant murine macrophage colony-stimulating factor (M-CSF), and recombinant murine granulocyte-macrophage colony-stimulating factor (GM-CSF) were obtained from ABclonal (Wuhan, China). Interleukin-4 (IL-4) and interferongamma (IFN- γ) were obtained from Peprotech (USA). Lipopolysaccharide (LPS) and DNase I were from Sigma-Aldrich (USA). Dulbecco's modified Eagle's Medium (DMEM) cell culture medium, PBS, Annexin V-FITC/PI apoptosis detection Kit, and terminal deoxynucleotidyl transferasemediated dUTP Nick end labeling (TUNEL) apoptosis assay kit were from Dalian Meilun Biotechnology Co., Ltd. (Dalian, China). Coomassie blue fast staining, color PAGE gel rapid preparation kit, and multicolor prestained protein ladder were from Epizyme Biotech Co., Ltd. (Shanghai, China). 3-(4, 5-dimethylthiazol-2-yl)-2, 5-diphenyltetrazolium bromide (MTT) was from Solarbio Science & Technology Co., Ltd. (Beijing, China). APC-Cy7 conjugated CD45, PE-Cy7 conjugated CD11b, PE conjugated F4/80, Alexa Fluor 647 conjugated CD206, BV421 conjugated CD86, APC conjugated CD4, FITC conjugated Ly-6-G and LY-6C, PE-Cy7 conjugated CD8a, BV421 conjugated CD25, BV605 conjugated CD80, and BV650 conjugated IFN- γ were obtained from BD Bioscience (USA). Brilliant Violet 421TM conjugated Ki-67 and PerCP/Cyanine5.5 conjugated CD11c were from Biolegend (USA).

BALB/c mice (female, 5–6 weeks) were provided by Shanghai Super B&K Laboratory Animal Corporation Ltd. (Shanghai, China) and housed at the SPF care facility. All the animal procedures were approved by the Institutional Animal Care and Use Committee (IACUC), Shanghai University of Traditional Chinese Medicine (PZSHUTCM2306280003) and the Institutional Animal Care and Use Committee of Shanghai Model Organisms (2023–0040).

The mouse TNBC cell line (4T1), human TNBC cell line (MDA-MB-468) and human umbilical vein endothelial cells (HUVECs) were obtained from the Shanghai Cell Bank of Chinese Academy of Sciences (Shanghai, China). All the cells were cultured in DMEM medium with 10 % FBS and streptomycin (100 U/ml)-penicillin (100 U/ml) in a humidified $5 \% CO_2$ incubator at $37 \degree C$.

2.2. Gene expression and immune correlation database analysis

SOS1 mRNA expression in normal and breast cancer tissues was examined via the TCGA database (https://portal.gdc.cancer.gov/), and then visualized via the Xiantao tool (https://www.xiantao.love/). Overall survival analyses of patients with breast cancer were performed using the Kaplan-Meier plotter (http://kmplot.com/analysis/). In addition, we further explored the correlation between SOS1 mRNA and macrophages in breast cancer. Additionally, the Cancer Imaging Archive (TCIA) (https://tcia.at/cellTypeFractions) was used to analyze immune cell proportions in Breast Cancer (BRCA), and Tumor Immune Estimation Resource (TIMER2.0, http://timer.cistrome.org/) provided a platform for analyzing

the relationship between overall survival rates and M1/M2 macrophages in BRCA patients.

2.3. SOS1 expression in normal and TNBC cells

Total RNA was isolated from cells with Trizol RNAisoPlus. Subsequently, RNA was reverse transcribed via a cDNA Reverse Transcription Kit. For real-time quantitative polymerase chain reaction (qRT-PCR), the cDNA was then amplified with primers and SYBR Green PCR Master Mix. PCRs were performed using Applied Biosystems (Thermo Fisher, USA). In addition, orthotopic 4T1 bearing tissues and normal mammary fat pads were extracted for SOS1 mRNA analysis. All primers were designed for the following genes:

Human SOS1 F-GAGTGAATCTGCATGTCGGTT, Human SOS1 R-CTCTCATGTTTGGCTCCTACAC, Human GAPDH F-GTCTCCTCTGACTTCAACAGCG, Human GAPDH R-ACCACCCTGTTGCTGTAGCCAA, Mouse SOS1 F-CCTGCGCTGAAAAAGGTTCA, Mouse SOS1 R-AACACGTTCCTCCACATCTGA, Mouse β -actin F-CACTGTCGAGTCGCGTCC, Mouse β -actin R-TCATCCATGGCGAACTGGTG.

2.4. SOS1 inhibition by TET and the optimum ratio of TET/DTX

The inhibition of SOS1 by TET was detected via western blotting. Briefly, 4T1 cells were inoculated in 6-well plates $(2\times10^5~cells/well)$ and cultured for 24 h. The cells were treated with TET (100, 200, 500 nM) for 48 h, respectively. The cells were collected for SOS1 expression via western blot analysis. The optimum ratio of TET to DTX was determined via MTT assay in 4T1 cells. 4T1 cells were cultured in 96-well plates $(5\times10^3~cells/well)$. After 12 h of incubation, the culture medium was replaced with TET or DTX at different molar ratios for 48 h. Then MTT was added (12 mM) to each well, and the formazan crystals were dissolved in DMSO. The cell viability was measured by the absorbance at 490 nm using a Varioskan Flash multi-function reader (Thermo Fisher Scientific, USA). The synergistic effects of the drugs were evaluated using the following formula:

$$Cl = \frac{DX_{DTX}}{D_{DTX}} + \frac{DX_{TET}}{D_{TET}}$$

where D refers to IC50 of a single-dose and DX refers to IC50 of a combination-dose.

2.5. Cell membrane extraction and synthesis of DSPE-mPEG2000-Cil

4T1 cells were grown to 80 % confluence and harvested, followed by centrifugation at 700 g. The cells were then subjected to a hypotonic lysing buffer (distilled water: PBS= 4:1, v/v, 1 mM PMSF) with stirring at 4 °C for 12 h. After centrifugation at 700 g, the supernatant was harvested and further centrifuged at 14,000 g for 1 h. Finally, the 4T1 cell membrane pellet was resuspended in PBS and stored at $-80\,^{\circ}\text{C}$.

Cil, DSPE-mPEG2000-NH₂, O-(7-Azabenzotriazol-1-yl)-N,N,N',N'-te-tramethyluronium hexafluorophosphate (HATU) and N,N-diisopropylethylamine (DIPEA) were mixed with N,N-dimethylformamide (DMF) and stirred at room temperature for 24 h (Cil:DSPE-mPEG2000-NH₂=1:1, mol/mol). The reaction mixture was recrystallized with ether at $-20~^{\circ}\text{C}$, and then centrifuged at 10,000 rpm for 5 min. Finally, the mixture obtained was dialyzed against deionized water using a dialysis bag (MWCO 2kDa) for 48 h. Cil was successfully conjugated to DSPE-mPEG2000-NH₂, as determined by ^{1}H -NMR spectroscopy.

2.6. Preparation of Cil-modified membrane fusion liposomes

Lipo@TD was prepared via the thin-film hydration method. Soy lecithin (40 mg), cholesterol (13.3 mg), DSPE-mPEG2000 (1.2 mg), and the optimum ratio of TET:DTX (5:1, mol/mol) were mixed with chloroform. The organic solvent was evaporated under reduced pressure using a rotary evaporator. The lipid film was hydrated with PBS (pH 7.4), sonicated at 120 W for 8 min, and then extruded through a 400 nm polycarbonate membrane. The free drugs were removed using an ultrafiltration device (MWCO 10 kDa). The Cillipo@TD was prepared similarly, with DSPE-mPEG2000-Cil added to the chloroform-dissolved phospholipids. The CCMlipo@TD was fabricated by hydrating the lipid film with a cell membrane solution instead of PBS. The CCM/Cil-lipo@TD was constructed by simultaneously replacing with DSPEmPEG2000-Cil and cell membrane solution. In addition, DiR-, DiD- or DiI-labeled liposomes were also constructed by adding DiR, DiD or DiI to the chloroform solution, respectively.

2.7. Characterization of CCM/Cil-Lipo@TD

The size, polydispersity index (PDI) and zeta potential of Lipo@TD, Cil-lipo@TD, CCM-lipo@TD and CCM/Cil-lipo@TD were measured using a Malvern Zetasizer (Malvern Panalytical, UK). The morphology of the liposomes was characterized using transmission electron microscope (TEM, Tecnai G2 Spirit 120 kV, FEI Technai, USA) after they were stained following phosphotungstic acid staining. For stability test, the size and PDI of the liposomes were measured after storage in PBS (pH 7.4) containing 10 % newborn bovine serum. The in vitro drug release behavior was determined via dialysis tubes (MWCO 8–14 kDa) in a medium of PBS (pH 7.4) containing Tween 80 (1 %, w/v). The encapsulation efficiency (EE) and drug-loading capacity (DL) of CCM/Cil-lipo@TD were determined by HPLC.

$$\mbox{EE(\%)} = \frac{\mbox{Weight of encapsulated drugs}}{\mbox{Total weight of added drugs}} \times 100\%$$

$$DL(\%) = \frac{\text{Weight of encapsulated drugs}}{\text{Weight of liposomes}} \times 100\%$$

Total protein analysis of Lipo@TD, Cil-lipo@TD, CCM-lipo@TD, CCM/Cil-lipo@TD and the cell membrane proteins was performed via sodium dodecyl sulfate-polyacrylamide gel electrophoresis (SDS-PAGE). The membrane proteins were extracted with RIPA lysis buffer, and further denatured with

loading buffer followed by heating to 95 °C. All the samples were separated on a 10 % SDS–PAGE gel using a Mini-PRO4 System (WIX, China), and then stained with Coomassie Blue. The gels were visualized with a Tanon imaging system (5200Multi, China). For western blot analysis, proteins were transferred onto a PVDF membrane, and then the expression of E-cadherin and Na $^+$ K $^+$ -ATPase was characterized using a Tanon imaging system.

2.8. Scratch wound and tube formation assay

For the scratch wound assay, HUVECs were plated into 6-well plates at a density of 1×10^5 cells per well. After cell attachment, the monolayer was scratched using a pipette tip and washed with PBS to eliminate detached cells. Then, the HUVECs were incubated with Cil (2 nM, 2 μ M), and DSPE-mPEG2000-Cil/phosphatide (Cil-lipo, 0.125 %, mol/mol) for 12 h, respectively. The scratch areas were imaged at 0 and 12 h, respectively. The area of the scratch wound was determined with ImageJ software (NIH, USA), and calculated as follows: Migration area = Area of the scratch wound at 0 h - Area of the scratch wound at 12 h.

Matrigel® was thawed and seeded in 96-well plates to solidify. Then, HUVECs were added onto polymerized Matrigel® plates and treated with Cil (2 nM) and Cil-lipo (2 nM). After incubation for 4 h, tube formation was analysed using an inverted microscope (Leica DMI6000B, Germany). The junction number and total tube length were calculated via ImageJ software.

2.9. Cellular uptake efficiency and in vitro cytotoxicity

For the homotypic targeting ability study, 4T1 or RAW264.7 cells were incubated with DiD-labeled liposomes for 1.5 h, and then stained with 4',6-Diamidino-2-phenylindole dihydrochloride (DAPI) for 10 min. Intracellular fluorescence was detected via a fluorescence microscope (ImageXpress Micro, Switzerland), and semi-quantified with ImageJ software (NIH, USA). In addition, the cellular uptake efficiency was detected by flow cytometry (BD LSRFortessa, USA). HUVECs and 4T1 cells were mixed at a ratio of 1:3, and then seeded in a 96-well plate with an ultra-low attachment and a round-bottom. The cells were cultured for 6 d to allow tumor spheroid formation. The tumor spheroids were incubated with DiD-labeled Lipo, Cil-lipo, CCM-lipo and CCM/Cil-lipo for 12 h, and then scanned via laser scanning confocal microscopy (ZeissLSM 710, Germany).

To assess in vitro cytotoxicity, 4T1 cells were cultured in 96-well plates at a density of 5 \times 10³ cells per well. The cells were then treated with TET, DTX, TET-DTX, Lipo@TD and CCM-lipo@TD (DTX:0, 1, 2.5, 5, 10, 15 nM), respectively. Cellular viability was determined via MTT assay using a Varioskan Flash full-wavelength scanning multi-function reader (Thermo Fisher Scientific, USA). 4T1 cell apoptosis was investigated via a FITC-Annexin V Apoptosis Detection Kit (MeilunBio®, China). 4T1 cells were seeded in 12-well plates at a density of 1.5 \times 10⁵ cells per well, and then treated with TET, DTX, TET-DTX, Lipo@TD and CCM-lipo@TD (equal to 50 nM TET and 10 nM DTX) for 24 h, respectively. Subsequently, the cells were collected and stained with Annexin V-FITC and PI

according to the protocol. The number of apoptotic cells was quantified via the flow cytometry.

2.10. Intracellular ROS, SOS1 and Bcl-xl expression

4T1 cells were treated with TET, DTX, TET-DTX, Lipo@TD and CCM-lipo@TD (equal to 25 nM TET and 5 nM DTX) for 24 h, respectively. For ROS detection, the cells were collected and quantified with a reactive oxygen detection kit (Beyotime Biotechnology, China). To further evaluate SOS1 and Bcl-xL expression, the cells were collected for western blot analysis.

2.11. Polarization of BMDMs

The bone marrow cells were generated from BALB/c mice following the standard protocol. Subsequently, the cells were cultured in DMEM medium (20 % FBS) containing 20 ng/ml M-CSF for 4 d, after which the medium was replaced with fresh medium containing either IFN- γ (20 ng/ml) and LPS (100 ng/ml) for TAM1 polarization or IL-4 (40 ng/ml) for TAM2 polarization. Subsequently, the cells were cultured in DMEM medium (20 % FBS) containing 20 ng/ml GM-CSF for 4 d. In the 4T1/BMDM transwell system, 4T1 cells were cultured in the upper chamber, while TAM2 cells were plated in the lower chamber. After 12 h of incubation, both cells were treated for 12 h with TET, DTX, TET-DTX, Lipo@TD and CCM-lipo@TD (equal to 25 nM TET and 5 nM DTX), respectively. In addition, M2 and M1 were used as controls, which provided baseline references to compare the effects of drug treatments (e.g., whether CCM-lipo@TD shifted TAM2 toward an M1-like phenotype). The expression of iNOS and Arg1 was analyzed via western blotting. The bone marrowderived macrophages (BMDMs) transwell model aimed to evaluate CCM-lipo@TD's ability to selectively "re-educate" TAM2 to a TAM1-like phenotype in the presence of 4T1 tumor cells.

2.12. ICD-induced DC maturation

For the ICD induction study, 4T1 cells were treated with TET, DTX, and TET-DTX (equal to 25 nM TET and 5 nM DTX) for 12 h, respectively. The cells were collected for staining with CRT antibody and Alexa Fluor 488, and then analyzed via a flow cytometer (Beckman CytoFLEX, USA). Simultaneously, the intracellular ATP levels were detected with an ATP assay kit (Beyotime Biotechnology, China). The bone marrow cells were generated using a standard protocol. The bone marrow-derived dendritic cells (BMDCs) were then differentiated into immature DCs with GM-CSF (20 ng/ml) and IL-4 (10 ng/ml), and co-incubated with the ICD-activated 4T1 cells for 24 h. The mature DCs (CD80+ CD86+) were characterized via the flow cytometry.

2.13. In vivo distribution and antitumor efficacy

DiD-labeled liposomes were constructed by adding DiD instead of TET and DTX to the chloroform solution. DiD exhibits a red-shifted fluorescence with excitation and emission spectra at 644 nm/665 nm (λ ex/ λ em). The fluorescence intensities (DiD) of liposomes could be detected

using an IVIS system (PerkinElmer, USA). 4T1 cells (1 \times 10⁶) were subcutaneously injected into the mammary fat pads of BALB/c mice. When the tumor volume reached 300-500 mm³, 4T1 tumor-bearing mice were intravenously injected with Cil-lipo@DiD, CCM-lipo@DiD and CCM/Cillipo@DiD. Biodistribution was monitored via an IVIS imaging system (PerkinElmer, USA). At 24h post-administration, the mice were sacrificed and the major organs (e.g., heart, liver, spleen, lung, kidney) and tumors were harvested for ex vivo imaging. For determination of the tumor distribution and angiogenesis of the liposomes, the tumor tissues were frozen in optimal cutting temperature compound (OCT), and then sliced using a Leica CM 1950 Cryostat (Leica, Germany). Then, tumor vessels were stained with a primary anti-CD31 antibody followed by an Alexa Fluor 488-conjugated secondary antibody. The fluorescence images were captured via a laser scanning confocal microscope (Olympus FV1200,

The established orthotopic TNBC models were randomly divided into 8 groups (5 mice per group). PBS, TET, DTX, TET-DTX, Lipo@TD, Cil-lipo@TD, CCM-lipo@TD and CCM/Cillipo@TD were injected intravenously at doses of 12 mg/kg TET and 3 mg/kg DTX (equivalent to a molar ratio of 5:1) once every 3 d for 4 cycles. DTX was dissolved in DMSO and then dispersed in 10 % hydroxypropyl- β -cyclodextrin (HP- β -CD). TET was dissolved in 1 mM HCl; then the pH was adjusted to neutrality with 0.5 mM NaOH and finally dispersed in 10 % HP- β -CD. The tumor volume and body weight were recorded at various time points. The tumor volume was calculated using the following relationship: Length \times Width \times Width/2. After 15 d of treatment, the mice were euthanized, and the major organs (heart, liver, spleen, lung and kidney) and tumors were harvested for weighing and hematoxylin and eosin (H&E) staining. Then, the serum was collected and separated for biochemical analysis of aspartate aminotransferase (AST), alanine transaminase (ALT) and total protein (TP). For mechanistic studies, the tumors were prepared for western blotting, flow cytometric analysis, TUNEL staining and immunofluorescence staining.

2.14. Western blot, TUNEL assay and flow cytometry

Following previously described procedures [26], we lysed cells and tumors with RIPA buffer supplemented with 1 % protease inhibitors. The total protein concentration was quantified with a BCA protein assay kit (Beyotime, China). Then, the protein samples were separated via SDS-PAGE electrophoresis, and then transferred onto polyvinylidene difluoride membranes. Afterward, the membranes were blocked with 5 % non-fat dried milk, and then incubated with the primary antibody overnight at 4 °C. Finally, the protein bands were incubated with the HRP-conjugated secondary antibodies, followed by detection using the ECL reagent.

A TUNEL assay was performed using the TUNEL Apoptosis Assay Kit according to the manufacturer's protocol. In brief, the tissue slices were deparaffinized, rehydrated, washed, and permeabilized. The slices were incubated with the TUNEL reaction mixture containing the enzyme terminal deoxynucleotide transferase (TdT) and FITC-12-dUTP Labeling Mix. Finally, the nuclei were stained with DAPI, and then

scanned via laser scanning confocal microscopy (Olympus Spin SR10, Japan).

On Day 15, the mice were euthanized, and the tumors and spleens were isolated. The tumors were mechanically dissociated using surgical scissors, and digested with DMEM containing DNase I, hyaluronidase, and collagenase IV. The spleens were mechanically ground and dispersed in erythrocyte lysis buffer. Sequentially, single cells from tumors and splenocytes were stained with Live Dead Fixable viability stain (BD, USA), followed by Fc block (BD, USA) and fluorescently labeled antibodies. TAM1 cells were stained with anti-mouse CD45, CD11b, F4/80 and CD86 antibodies. TAM2 cells were stained with anti-mouse CD45, CD11b, F4/80 and CD206 antibodies. DCs were stained with anti-mouse CD45, CD11b, CD11C, CD80 and CD86 antibodies. Myeloidderived suppressor cells (MDSCs) were stained with antimouse CD45, CD11b and Ly6C&Ly6G (Gr-1) antibodies. T lymphocytes were stained with anti-mouse CD45, CD3, CD4, CD8, IFN- γ , Granzyme B and Ki67 antibodies. Tregs were stained with anti-mouse CD45, CD3, CD4, CD25 and Foxp3 antibodies. Finally, the stained cell suspensions were analyzed using flow cytometry (BD LSRFortessa, USA).

2.15. Postsurgical recurrent tumor models and therapeutic scheme

For the 4T1 tumor recurrence model, 1×10^6 4T1-luc cells were injected into the left lower mammary pad of BALB/c mice. Twelve days after the mice were inoculated with 4T1 cells, the tumor tissues were resected by surgery, and ~ 1 % residual tumors were left to mimic residual tumors after surgery. The specific tumors were confirmed by bioluminescence of IVIS imaging system after intraperitoneal injection of the luciferin substrate. After surgery, PBS, TET-DTX and CCM/Cil-lipo@TD were administered according to the indicated schedule. The tumor volumes were monitored during the whole experiment, and survival after treatment was recorded. The lungs were excised, and the lung metastatic nodules were further observed using Bouin's staining. In addition, the lung tissues were stained with H&E, and then visualized using a Pannoramic SCAN (3DHISTECH, Hungary).

2.16. Statistical analysis

The statistics were analyzed by using GraphPad Prism 8.0. The Data are expressed as the means \pm SD ($n \ge 3$). Statistical significance was evaluated using a Student's t-test and was expressed as *P < 0.05, **P < 0.01, and ***P < 0.001.

3. Results and discussion

3.1. Overexpression of SOS1 in TNBC

Bioinformatic analysis was performed to examine the expression of SOS1 in breast invasive carcinoma using TCGA (https://cancergenome.nih.gov). We confirmed that SOS1 was significantly upregulated in basal-like subtypes (primarily TNBC) compared with normal adjacent tissues (Fig. 1A).

Also, higher SOS1 levels in Asian patients with breast cancer were significantly (P=0.0013) correlated with worse survival (http://kmplot.com/analysis/) (Fig. 1B). We then examined SOS1 mRNA levels in the TNBC cells and tumor tissues via qRT–PCR, which confirmed that SOS1 mRNA was indeed highly expressed in MDA-MB-468 cells and 4T1-bearing tumor tissues, respectively (Fig. 1C and D). These findings highlight the critical roles of SOS1 in TNBC progression.

3.2. Optimum ratio of TET/DTX combination

As shown in Fig. 1E and F, TET effectively inhibited SOS1 expression in a dose-dependent manner. Interestingly, TET has been reported to synergistically enhance the antitumor effect of chemotherapy drugs by reversing drug resistance [27] and inducing mitochondrial apoptosis [28]. DTX, a microtubule stabilizer, is a commonly used chemotherapeutic agent in clinical TNBC therapy [29]. The cytotoxicity of TET and DTX against 4T1 cells was examined via a MTT assay. As shown in Fig. 1G and H, the optimal ratios for synergistic activity were identified as 5:1 and 1:1 (TET:DTX, mol/mol), with combination index (CI) values of 0.604 and 0.638 (CI<1 revealed synergism), respectively. However, at the 1:1 ratio, DTX concentrations (5 nM) required to induce ICD failed to synergize with the TET-mediated SOS1 blockade. As a result, the 5: 1 molar ratio was determined as the optimal formulation.

3.3. Preparation and characterization of CCM/Cil-Lipo@TD

Briefly, the preparation of CCM/Cil-lipo@TD included four steps: (1) synthesize DSPE-mPEG2000-linked Cil via the reported protocols [30], and prepare Cil-lipo@TD coloaded with TET and low-dose DTX (5:1, mol/mol) via the thinfilm hydration method, (2) extract 4T1 cell membranes via a hypotonic method [31], and then fuse 4T1 cell membranes with Cil-lipo@TD, yielding CCM/Cil-lipo@TD (Fig. 2A). First, the structure of DSPE-mPEG2000-Cil was confirmed by ¹H NMR spectroscopy, with a Cil grafting rate of 15.5 % (Fig. S1). DSPE-PEG-Cil and DSPE-PEG had a peak of repeated units of PEG at 3.52 ppm, and peaks of DSPE at 1.24 ppm. Meanwhile, the phenyl ring peak of DSPE-PEG-Cil and Cil was detected at 7.21 ppm, confirming Cil incorporation. To optimize liposome-membrane fusion, we quantified the membrane protein (BCA assay), then evaluated the uptake efficiency of CCM-lipo@DiR in 4T1 cells across phospholipidto-cell membrane protein mass ratios (e.g., 40:1 to 5:1, w/w). As shown in Fig. 2B and C, greater red fluorescence was observed in CCM-lipo@DiR-treated-4T1 cells with the increment of cell membrane mass. Also, flow cytometry revealed the same trend of uptake (Fig. 2D and E). Notably, CCM-lipo@DiR at a 10:1 ratio (w/w) exhibited significantly smaller hydrodynamic diameters than the 5:1 ratio (w/w) (Fig. S2A), which might result in better capture by tumor tissues. As a result, the 10:1 ratio (w/w) was selected to balance size and uptake efficiency. Additionally, the successful fusion of 4T1 cell membranes and liposomes was further verified via the Förster resonance energy transfer (FRET) technique. Considering that the FRET requires a very close distance (<10 nm) between the donor

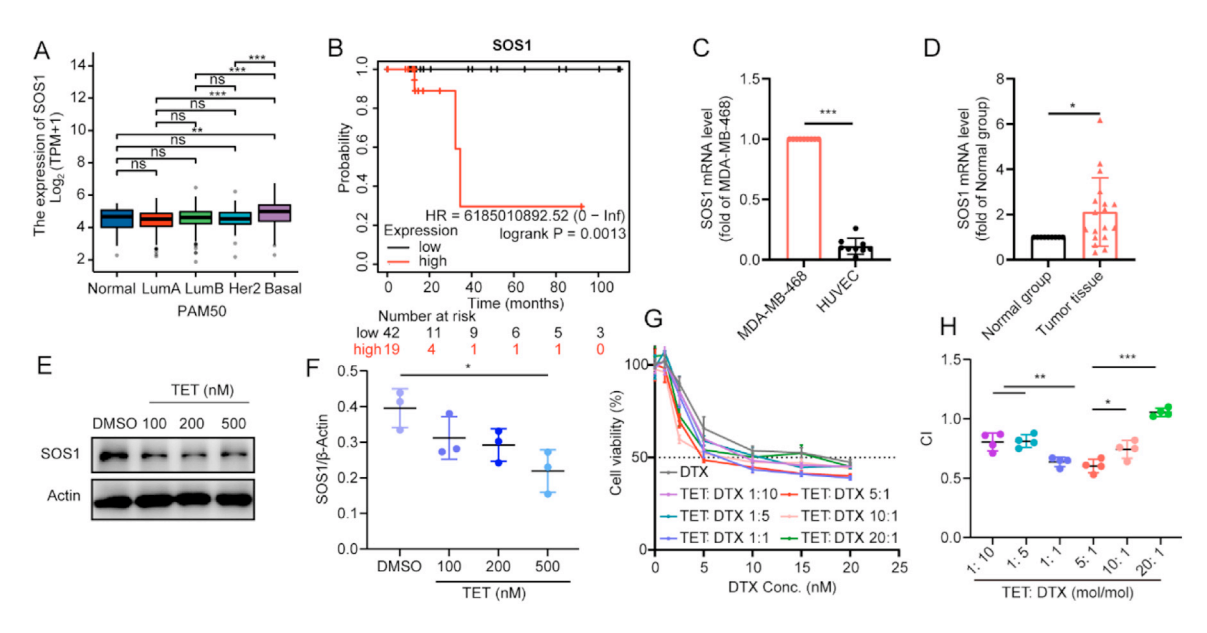


Fig. 1 – SOS1 was activated in breast cancer and the optimum ratio of the TET/DTX combination was determined. (A) Bioinformatic analysis of SOS1 expression in normal tissues and breast cancer tissues (TCGA database); (B) Correlation analysis between SOS1 and the survival in breast cancer patients (TCGA database); (C) Comparison of SOS1 mRNA between HUVEC lines (normal) and MDA-MB-468 cells (tumor cells) by qPCR; (D) Comparison of SOS1 mRNA between normal tissues and orthotopic 4T1 tumor tissues by qPCR; (E and F) SOS1 expression was inhibited by TET (n = 3); (G) Optimal synergistic ratio and (H) quantitative analysis of TET and DTX via MTT (n = 4). *P < 0.05, **P < 0.01 and ***P < 0.001.

(DiI) and acceptor (DiD), the lipid was dual-labeled with DiI (Ex/Em: 549 nm/565 nm) and DiD (Ex/Em: 644 nm/665 nm) (the mass of DiI is equivalent to DiD, CCM-lipo@DiI&DiD). When liposomes fused with CCMs, the increased donor-acceptor distance significantly compromised FRET efficiency [32]. As shown in Fig. S2B, when the CCM-lipo@DiI&DiD was excited at 510 nm, the fluorescence at 565 nm decreased with reducing 4T1 cell membrane mass, suggesting that there was a FRET effect between the donor (DiI) and acceptor (DiD) due to longer distances (greater than 10 nm). The FRET results revealed that 4T1 cell membranes were successfully fused with the liposomes.

Based on this, breast CCM-fused liposomes embedded with TET and DTX were prepared, and then engineered with Cil to generate CCM/Cil-lipo@TD. The TEM image of CCM/Cil-lipo@TD showed a spherical morphology (Fig. 2F), consistent with Cryo-TEM results (Fig. S2C). Moreover, the average hydrodynamic diameter of CCM/Cil-lipo@TD was 124.5 \pm 5.5 nm (PDI<0.2), and the zeta potential was -11.3 ± 0.8 mV similar to the surface charge of 4T1 cell membranes, which further revealed successful membrane fusion (Fig. 2G and H, Table S1). Interestingly, compared with that of Lipo@TD, the zeta potential of Cil-modified liposomes (Cil-lipo@TD) exhibited a less negative zeta potential (-7.5 ± 0.2 mV), likely attributable to the protonated guanidinium moieties of Cil (Table S1). The EE of TET and DTX were 65.4 % \pm 2.5 % and 66.1 % \pm 0.1%, respectively, and the DL ratio was \sim 5:1 (TET:DTX) (Table S2). Compared with those of the 4T1 cell membrane lysate, the protein profiles of CCM-lipo@TD and CCM/Cil-lipo@TD were well preserved via SDS-PAGE-Coomassie staining (Fig. 2I). The CCM/Cil-lipo@TD was stable in 10 % serum-containing PBS (Fig. 2J and K) and showed a sustained release of both TET and DTX (Fig. 2L and M). The in vitro drug release rate of the TET and DTX in the CCM/Cil-lipo@TD was 82.0 % and 86.0 % at 24 h, with a consistent 5:1 molar ratio throughout the release profile. Western blot analysis further revealed that CCM-lipo@TD and CCM/Cil-lipo@TD possessed specific protein markers (e.g., E-cadherin and Na $^+$ K $^+$ -ATPase) of 4T1 cell membranes (Fig. 2N). Additionally, the hemolysis of CCM/Cil-lipo@TD in red blood cell suspensions was <5 %, confirming excellent biocompatibility (Fig. 2O).

3.4. In vitro tumor targeting and Cil-based vascular promotion capacity of CCM/Cil-lipo

The CCM-lipo@DiD and CCM/Cil-lipo@DiD groups showed significantly higher cellular internalization than Lipo@DiD in 4T1 monolayer cells, whereas Cil-lipo@DiD showed no improvement (Fig. 3A, B and S3A, S3B). The reduced cellular uptake of CCM/Cil-lipo@DiD compared to CCMlipo@DiD in 4T1 cells (Fig. S3A and S3B) may involve several potential mechanisms. Specifically, CCM-lipo@DiD inherits homologous membrane proteins from cancer cells, enabling "self-recognition" mechanisms via membrane fusion or phagocytosis to enhance uptake [23]. In contrast, as an $\alpha v \beta 3/\alpha v \beta 5$ integrin antagonist, Cil may block integrinmediated endocytosis pathways rather than uptake promotion [33]. To confirm this feature, we checked the NP uptake capacities of normal cells (RAW264.7). The results suggested that although CCM-lipo@DiD showed better uptake by 4T1 cells (as shown in Fig. 3A and B), it showed lower

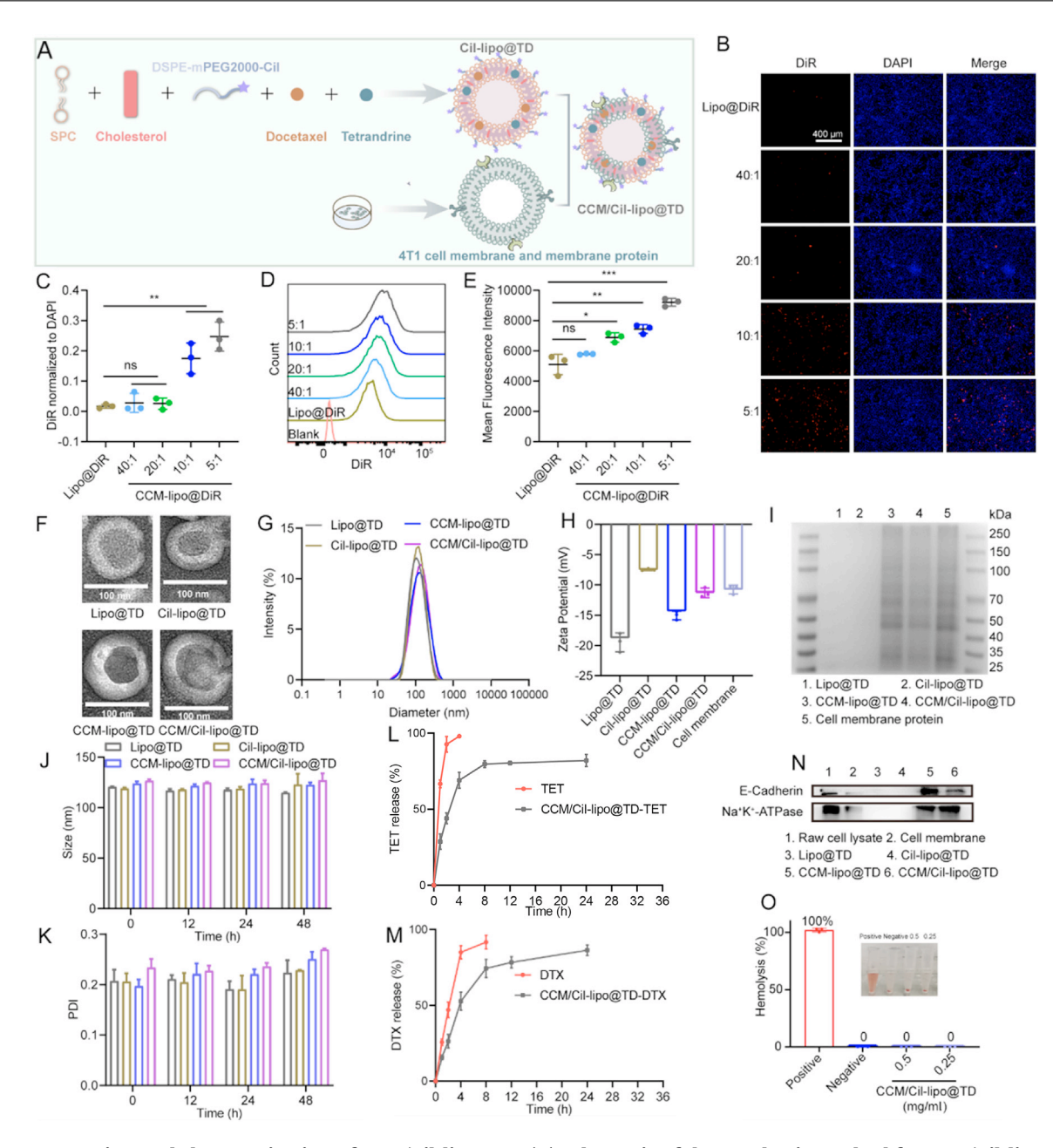


Fig. 2 – Preparation and characterization of CCM/Cil-lipo@TD. (A) Schematic of the synthesis method for CCM/Cil-lipo@TD. SPC: soy lecithin; (B) Fluorescence image and (C) quantitative results of 4T1 cells incubated with CCM-lipo@DiR (with different mass ratio of phospholipid to the cell membrane). The nuclei were stained with DAPI (blue) and the liposomes were labeled with DiR (Red). Scale bar: 400 μ m; (D) Flow cytometric analysis and (E) quantitative results of the cellular uptake of CCM-lipo@DiR. (F) TEM (120 kV) images of different liposomes. Scale bar: 100 nm; (G) Particle size distribution and (H) zeta potential of the liposomes; (I) SDS-PAGE/Coomassie staining of liposomes and cell membrane proteins; (J and K) Stability of liposomes in PBS containing 10 % serum. In vitro release of (L) TET and (M) DTX from CCM/Cil-lipo@TD; (N) Western blot analysis of specific proteins (E-cadherin and Na+K+-ATPase) in the raw cell lysate, cell membrane and liposomes; (O) Hemolytic characteristics of CCM/Cil-lipo@TD (n = 3). *P < 0.05, **P < 0.01, ***P < 0.001.

fluorescence intensity than Lipo@DiD in RAW 264.7 cells, indicating selected targeting to homotypic 4T1 cells (Fig. S3C and S3D). It has been reported that Cil has dual effects on vessels [33,34]. On the one hand, micromolar concentrations of Cil have antiangiogenic effects by blocking the binding of $\alpha v \beta 3$ to the extracellular matrix [33]. On the other hand,

nanomolar concentrations of Cil can promote vascular endothelial growth factor (VEGF)-mediated angiogenesis [34]. To further interrogate these concentration-dependent effects, we performed migration and tube formation assays using HUVECs. Quantitative analysis demonstrated that 2 nM Cil displayed a promoting effect on HUVEC migration, whereas

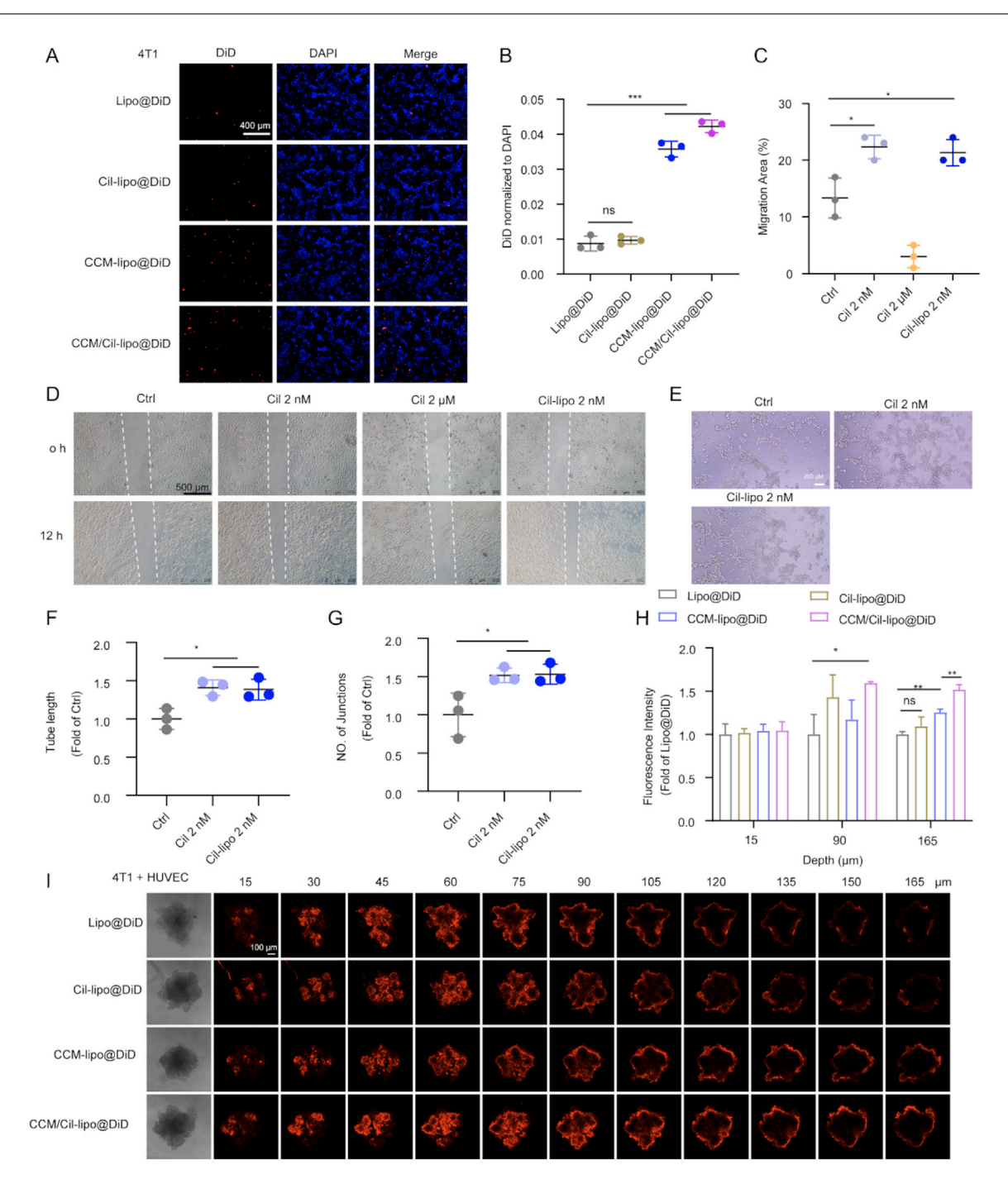


Fig. 3 – CCM/Cil-lipo@DiD promoted cellular uptake and tumor spheroid penetration in vitro. (A) Fluorescence image and (B) semiquantitative analysis of 4T1 cells after incubation with liposomes. Scale bar: 400 μ m; (C, D) Micrographs of HUVEC migration at 0 and 12 h and semiquantitative analysis of the migration area after drug treatment. Scale bar: 500 μ m; (E) Micrographs of HUVEC tube formation and semiquantitative analysis of (F) total tube length and (G) junction number after 4 h of incubation with cilengitide and Cil-lipo (2 nM). Scale bar: 200 μ m; (H and I) CLSM images of the in vitro penetration of DiD-labeled liposomes in 4T1/HUVEC co-culture tumor spheroids and semiquantitative analysis of fluorescence intensity at 15, 90 and 165 μ m (n = 3). Scale bar: 100 μ m. *P < 0.05, **P < 0.01, ***P < 0.001.

 $2~\mu M$ treatment exerted a high antimigration effect. Moreover, Cil-lipo (with low-density Cil)-treated HUVECs presented a significantly greater migration area than the control group (P < 0.01), and were comparable to the Cil (2 nM)-treated group, indicating the HUVEC migration promoting function

(Fig. 3C and D). Tube formation assays were further employed to examine the proangiogenic ability of Cil-lipo. Compared to the control, Cil-lipo and Cil (2 nM) induced a significantly greater increment of the junction number and tube length, suggesting a promoting effect on tube formation (Fig. 3E–G).

These findings altogether confirmed that Cil-lipo may exert penetration promotion via enhanced HUVEC migration and improved tube formation at nanomolar concentrations of Cil. Later, a 4T1/HUVEC spheroid model was established to investigate the intratumoral permeability of CCM/Cillipo@DiD in vitro. Confocal laser scanning microscopy (CLSM) results revealed that the CCM/Cil-lipo@DiD group showed much deeper infiltration than the Lipo@DiD and CCM-lipo@DiD groups at a 165 μm scanning depth (Fig. 3H and I). Collectively, the tumor accumulation of CCM/Cillipo@DiD was significantly improved with the aid of tumor cell membrane-triggered homologous targeting and Cilmediated penetration promotion.

3.5. CCM-lipo@TD exhibited cytotoxicity in 4T1 cells and induced DC maturation

The half-maximal inhibitory concentration (IC50) of free TET-DTX in 4T1 cells was 9.5 nM (indicated by the DTX concentration, Fig. 4A and B), whereas CCM-lipo@TD showed the highest antitumor efficacy (IC50: 7.6 nM, indicated by the DTX concentration) compared to other groups. Moreover, CCM-lipo@TD enhanced ROS production (1.5-fold higher than that of free TET-DTX, Fig. 4C and D). An apoptosis assay further confirmed the proapoptosis superiority of the CCM-lipo@TD group, inducing 5.7-fold and 2.0-fold greater apoptosis rates compared to PBS and TET-DTX groups, respectively (Fig. 4E and F). In addition, CCM-lipo@TD reduced the expression of Bcl-xl (antiapoptosis protein, Fig. 4G and H).

ICD promotes the release of tumor-associated antigens (TAAs) and damage-associated molecular patterns (DAMPs), characterized by CRT eversion, high mobility group box 1 (HMGB1) release, as well as adenosine triphosphate (ATP) secretion [35]. CRT acts as an "eat me" signal to elicit phagocytosis by DCs, while HMGB1 and ATP elicit DC maturation and present TAAs to naive T-cells, thus promoting infiltration of tumor lymphocytes for tumor killing [36]. Interestingly, TET monotherapy did not significantly change in CRT or ATP secretion. However, our results demonstrated the ICD effect of low-dose DTX on 4T1 cells, as indicated by increased CRT (1.4-fold higher than that of the control) and decreased intracellular ATP levels (decreased by 15 % compared to control) (Fig. 4I-4K), which was consistent with previous reports [37]. TET-DTX further enhanced the ICD effect. DCs can present tumor antigens to naive T cells, thereby initiating effective adaptive immune responses [38]. In accordance with the increased ICD effect, CCM-lipo@TDtreated 4T1 cells significantly promoted BMDC maturation (costimulatory molecules, CD80+ CD86+), with 1.3-fold higher effects compared to TET-DTX and Lipo@TD, respectively (Fig. 4L-4N).

Overall, CCM-lipo@TD significantly inhibited 4T1 cell proliferation through the induction of cell apoptosis and ICD, resulting in excellent antitumor efficacy in vitro.

3.6. CCM-lipo@TD inhibited SOS1 expression and induced macrophage repolarization

Our results also demonstrated that TET monotherapy induced a 36.7 % reduction in SOS1 expression versus controls (Fig. 4G

and O), while CCM-lipo@TD treatment further resulted in a 43.0 % lower expression of SOS1 than TET alone. It was reported that high SOS1 expression promoted TAM2 polarization [15]. Macrophages in the TME, also known as TAMs, can be induced into an anti-tumor (so-called TAM1-like) or a pro-tumor (so-called TAM2-like) phenotype [39]. TAM2 leads to the formation of a suppressive TME [40]. Our results showed that TAM2 was reversed by CCM-lipo@TD in the M2Φ/4T1 transwell models (Fig. 4N), as reflected by the increment of M1-related markers (e.g., inducible nitric oxide synthase, iNOS, Fig. 4P and Q) and the downregulation of the M2-related markers (e.g., Arg1, Fig. 4P and R). Taken together, these results suggested that CCM-lipo@TD could downregulate SOS1 expression, thereby repolarizing TAM2 to TAM1.

3.7. Cil improved tumor penetration and CCMs enhanced tumor targeting in 4T1 orthotopic models

To investigate the tumor penetration ability after Cil modification, the in vivo and ex vivo distributions of the DiD-labeled liposomes were investigated using the IVIS imaging system. Cil-lipo@DiD demonstrated rapid and sustained accumulation in 4T1-bearing tumor areas at 2 h, 5 h and 24 h post-injection (Fig. S4A and S4B). Ex vivo imaging further revealed that the fluorescence intensity of Cil-lipo@DiD was 1.4-fold higher than that of Lipo@DiD (Fig. S4C and S4D). Moreover, immunofluorescence staining further confirmed that Cil-lipo@DiD was widely distributed in tumor slices, whereas Lipo@DiD remained localized to peripheral regions (Fig. S4E), indicating that Cil modification significantly improved tumor penetration.

CCMs expressing surface adhesion molecules have been used for drug delivery to tumor tissues through a tumorhoming effect [41]. CCM-mediated homologous targeting has been demonstrated in other studies [42,43]. CCMs can incorporate various cell-surface proteins that confer nanoparticles with certain properties such as the ability to avoid rejection by the immune system, which reduces the possibility of off-target effects on normal cells [23]. The TNBC-targeting ability of CCM/Cil-lipo@DiD was subsequently investigated in a 4T1-bearing mouse model. As shown in Fig. 5A and B, CCM/Cil-lipo@DiD resulted in greater tumor accumulation than Cil-lipo@DiD and CCM-lipo@DiD after injection (e.g., 2 h, 5 h and 24 h). Ex vivo imaging further revealed that the fluorescence intensities of CCM/Cillipo@DiD were 1.5-fold and 1.6-fold higher than those of Cillipo@DiD and CCM-lipo@DiD, respectively (Fig. 5C and D). Furthermore, the ex vivo CLSM results showed that CCM/Cillipo@DiD was widely distributed in tumor slices, consistent with the findings of Cil-lipo@DiD (Fig. 5E). As the scanning depth increased, CCM/Cil-lipo@DiD could deeply permeate to distant tumor areas, indicating the intratumoral penetration capacity. In addition, strong fluorescence intensities were detected in the tumor sections of the CCM/Cil-lipo@DiD group, supporting the observation that CCM/Cil-lipo@DiD had a strong tumor targeting efficiency (Fig. 5F and G). More specifically, CD31 immunostaining revealed comparable vascular density in tumors treated with CCM/Cil-lipo@DiD and Cil-lipo@DiD (Fig. 5F and H), which might be due to

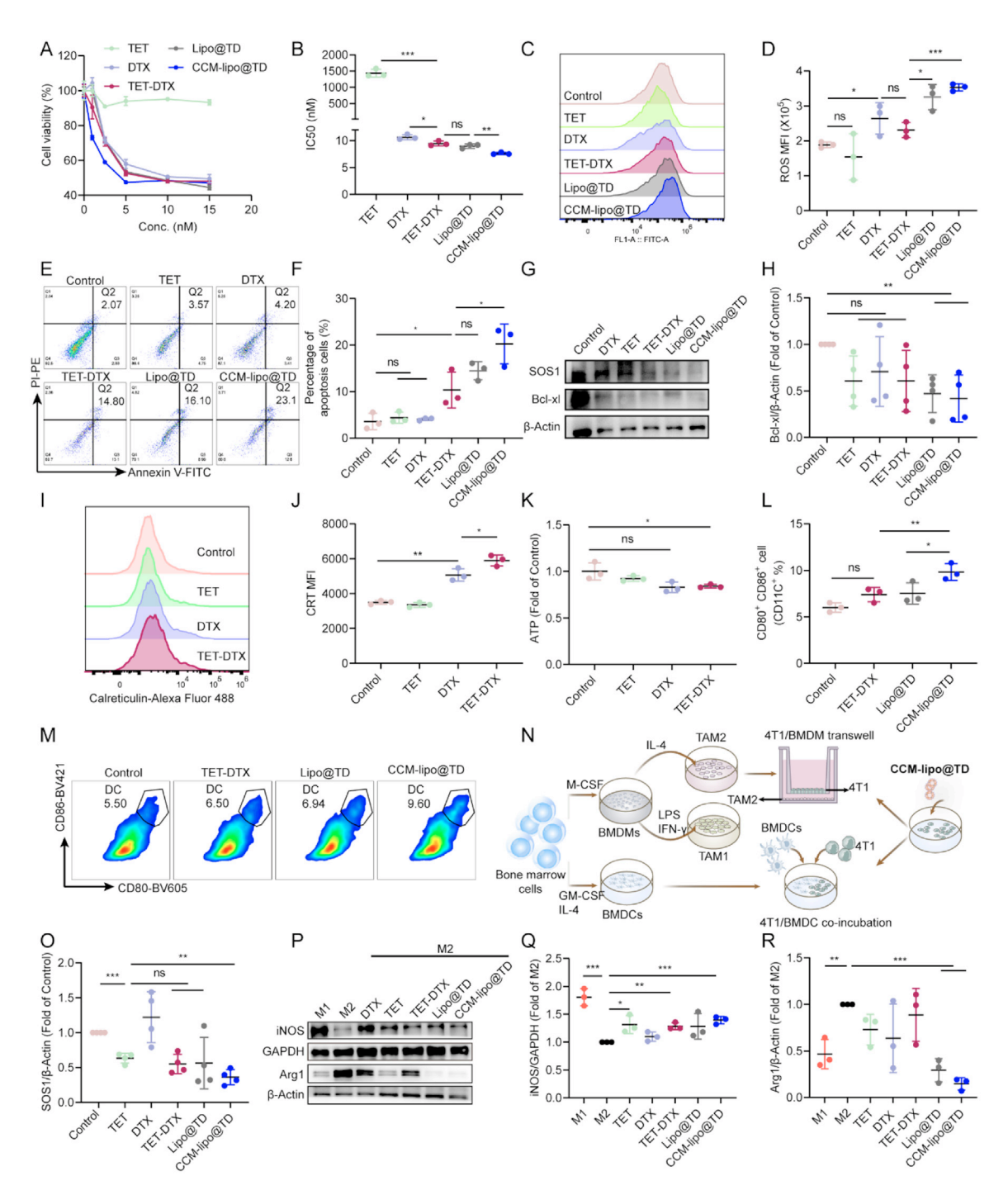


Fig. 4 – In vitro proapoptosis and immune activation by CCM-lipo@TD-induced ROS, TAM2 repolarization and DC maturation. (A and B) MTT assay of 4T1 cells (n = 3); (C) Flow cytometric histograms and (D) quantitative analysis of ROS levels in 4T1 cells (n = 3); (E) Apoptosis assay and (F) quantitative analysis of apoptotic 4T1 cells via flow cytometry (n = 3); (G) Western blot analysis and semiquantitative analysis of (H) Bcl-xL and (O) SOS1 expression in 4T1 cells (n = 4); (I) Flow cytometric histograms and (J) quantitative analysis of CRT exposure in 4T1 cells (n = 3); (K) Intracellular ATP levels (n = 3); (L and M) Flow cytometric histograms and quantitative analysis of DC (CD80+ CD86+) subsets stimulated by CCM-lipo@TD induced ICD (n = 3); (N) BMDM repolarization and ICD-induced BMDC maturation after CCM-lipo@TD treatment (n = 3); (P to R) Western blot analysis and semiquantitative analysis of M1-related markers (e.g., iNOS) and M2-related markers (e.g., Arg1) in BMDMs co-cultured with 4T1 cells after various treatments (n = 3). *P < 0.05, *P < 0.01, ***P < 0.001.

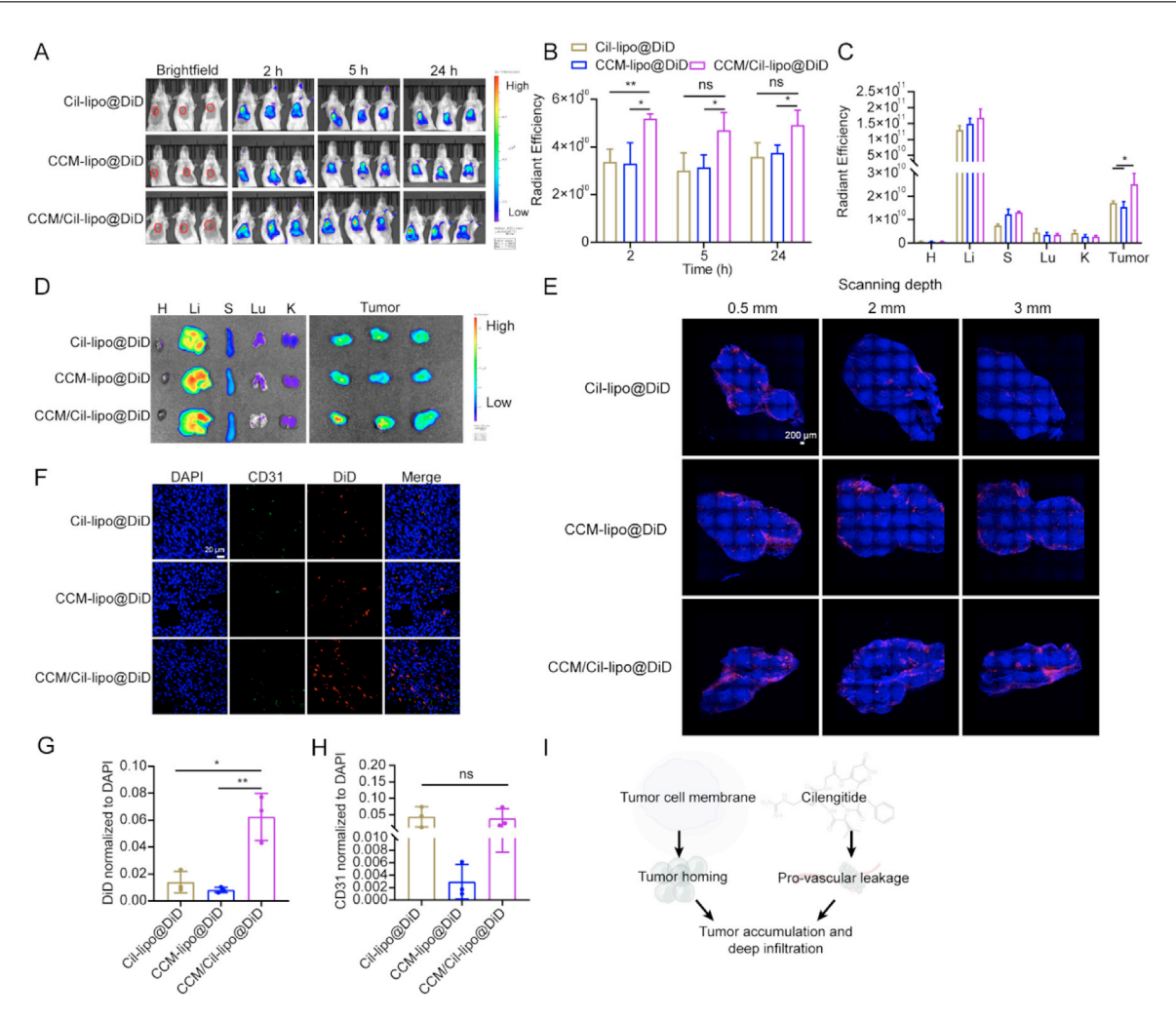


Fig. 5 – CCM/Cil-lipo@DiD displayed improved intratumoral distribution in an orthotopic 4T1 tumor model. (A) Body imaging; (B) Radiant efficiency analysis of liposomes accumulated in breast tumor tissues in vivo; (C and D) Ex vivo imaging and semiquantitative analysis of major organs and tumor tissues. H: heart, Li: liver, S: spleen, Lu: lung, K, kidney; (E) CLSM images of the distribution of CCM/Cil-lipo@DiD (red) in tumor tissues. The nuclei were stained with DAPI (blue). Scale bar: $200~\mu\text{m}$; (F) Fluorescence images of DiD-labeled liposomes in slices of tumor tissues. The blood vessels were stained with an anti-CD31 antibody (green). Scale bar: $20~\mu\text{m}$; Semiquantitative analysis of (G) DiD and (H) CD31 expression; (I) Effects of CCM/Cil-lipo@DiD on tumor accumulation and deep infiltration (n = 3). *P < 0.05, **P < 0.01.

the vascular promotion capacity and enhanced penetration promotion of low-density Cil.

As shown in the schematic diagram of Fig. 5I, CCM/Cillipo@DiD mainly accumulated within the tumor site and permeated deeply into tumor tissues, owing to the homologous targeting of the tumor cell membrane and the superior penetration capability of low-dose Cil.

3.8. CCM/Cil-lipo@TD inhibited tumor growth in 4T1 orthotopic models

Given the superior targeting and penetrating ability of CCM/Cil-lipo@TD, its antitumor efficacy was evaluated in a 4T1-bearing TNBC mouse model. The tumor-bearing mice were injected with PBS, TET (12 mg/kg), low-dose DTX (3 mg/kg), TET-DTX (TET 12 mg/kg, DTX 3 mg/kg), Lipo@TD,

Cil-lipo@TD, CCM-lipo@TD, and CCM/Cil-lipo@TD (equivalent to a dosage of 12 mg/kg TET and 3 mg/kg DTX), respectively (Fig. 6A). The free drugs had limited therapeutic effects on tumor growth, with inhibition rates of 29.7 % (TET), 19.4 % (DTX) and 29.3 % (TET-DTX). In contrast, after they were loaded into liposomes, Lipo@TD significantly reduced tumor growth, with inhibition rates of 45.0 %. However, Cil-lipo@TD and CCMlipo@TD groups showed efficacy comparable to the Lipo@TD group (Fig. 6B-D), owing to insufficient tumor targeting and penetration. Notably, the dual-functional CCM/Cillipo@TD treatment displayed superior tumor inhibition (82.9 %). For H&E staining of the tumor slices, the CCM/Cillipo@TD group showed the largest necrotic areas (Fig. 6E). Moreover, the TUNEL assay revealed enhanced apoptosis induction (Fig. S5), correlated with Bcl-xl downregulation (antiapoptosis protein, Fig. 6F and G). Furthermore, CCM/Cil-

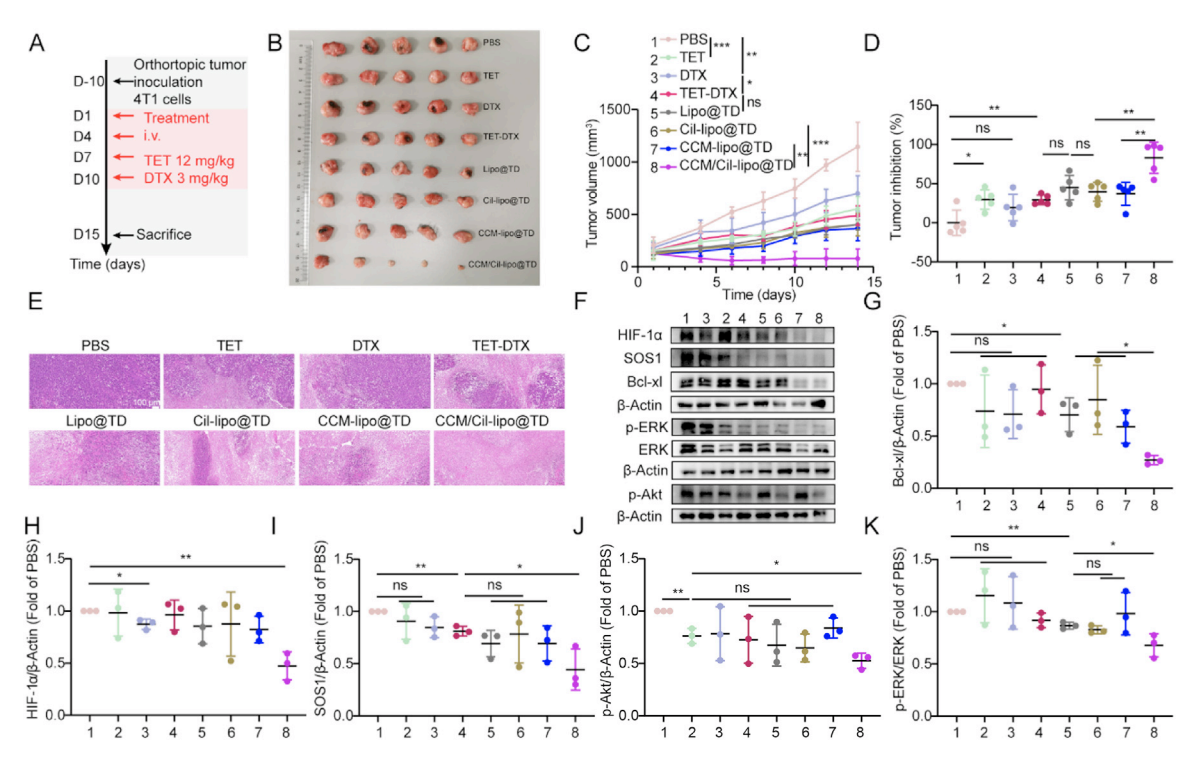


Fig. 6 – CCM/Gil-lipo@DiD restricted tumor growth in 4T1 orthotopic tumor-bearing mice, and exerted synergistic effects on SOS1 inhibition, DTX-induced ICD, and tumor hypoxia alleviation in vivo. (A) Therapeutic schedule. (B) Photos of the tumors harvested at the endpoint. (C) Tumor growth curves during treatment (n = 5). (D) The tumor inhibition rate (n = 5). (E) H&E staining of tumor tissues. Scale bar: 100 μ m (F) Western blot analysis and semiquantification of (G) Bcl-xL, (H) HIF-1 α , (I) SOS1, (J) p-Akt, (K) p-ERK expression in tumor tissues after different treatments (n = 3). *P < 0.05, *P < 0.01, ***P < 0.001.

lipo@TD efficiently alleviated hypoxia, as indicated by decreased hypoxia-inducible factor- 1α (HIF- 1α) expression (Fig. 6F and H).

Moreover, preliminary toxicity was investigated through H&E staining of major organs and blood biochemistry. The body-weight loss in the TET-DTX group was due to certain systemic toxicity of the free drugs and the tumor burden in 4T1-bearing mice (Fig. S6A). Importantly, low-dose DTX reduced toxicity in normal tissues (Fig. S6B) compared with traditional chemotherapies (e.g., 5 or 10 mg/kg) [44,45]. As shown in Fig. S6B, CCM/Cil-lipo@TD treatment normalized splenomegaly in 4T1-bearing mice. Furthermore, there was no significant change in the TP content in any of the groups (Fig. S6C), indicating no liver damage. In addition, after TET-DTX treatment, the serum biochemistry markers (e.g., AST and ALT) were higher than those in PBS-treated mice. In contrast, no obvious variation was observed in the CCM/Cillipo@TD group (Fig. S6D and S6E). In addition, the H&E staining results showed that systemic administration of DTX, TET-DTX, and Lipo@TD increased the number of inflammatory cells in the liver, indicating liver injury. However, no obvious side effects were observed in the CCM/Cil-lipo@TD-treated group (Fig. S6F). This safety profile may be attributed to the fact that the membrane fusion liposomes are designed to be biodegradable. No significant long-term accumulation of liposome components in the body, reducing the risk of longterm toxicity. Furthermore, Fig. 5 has demonstrated that the liposomes exhibited a high affinity for the tumor tissues and show minimal binding to non-target tissues. Taken together, these results were a preliminary confirmation of the biosafety of CCM/Cil-lipo@TD.

3.9. CCM/Cil-lipo@TD sufficiently downregulated SOS1 expression and reshaped the immunosuppressive TME of 4T1 orthotopic tumors

Western blot analysis also revealed differential SOS1 suppression across treatment groups. Compared to the PBS group, TET-DTX combination therapy significantly reduced SOS1 expression in tumor tissues, whereas CCM/Cillipo@TD further enhanced the inhibition efficiency (Fig. 6F and I). Other studies have demonstrated that SOS1mediated RAS activation promotes the phosphorylation of AKT and ERK, ultimately causing the activation of ERK and PI3K/AKT pathways [46]. We also found that the phosphorylation of Akt and ERK was effectively inhibited by CCM/Cil-lipo@TD treatment (Fig. 6F, J and K), which is consistent with previous reports that SOS1 activates the Akt and ERK signaling pathway [47,48]. Besides, tumor cellderived extracellular vesicles can promote M2 macrophage recruitment through various signaling pathways (e.g., PI3K/Akt, and MAPK/ERK) [49]. Furthermore, emerging evidence suggests that the SOS1/Akt and SOS1/ERK signaling pathways are associated with the regulation of TAM2 polarization [15]. In addition, the TCGA database revealed a significant positive correlation between SOS1 expression and macrophage infiltration in breast-invasive carcinoma patients (Fig. S7A).

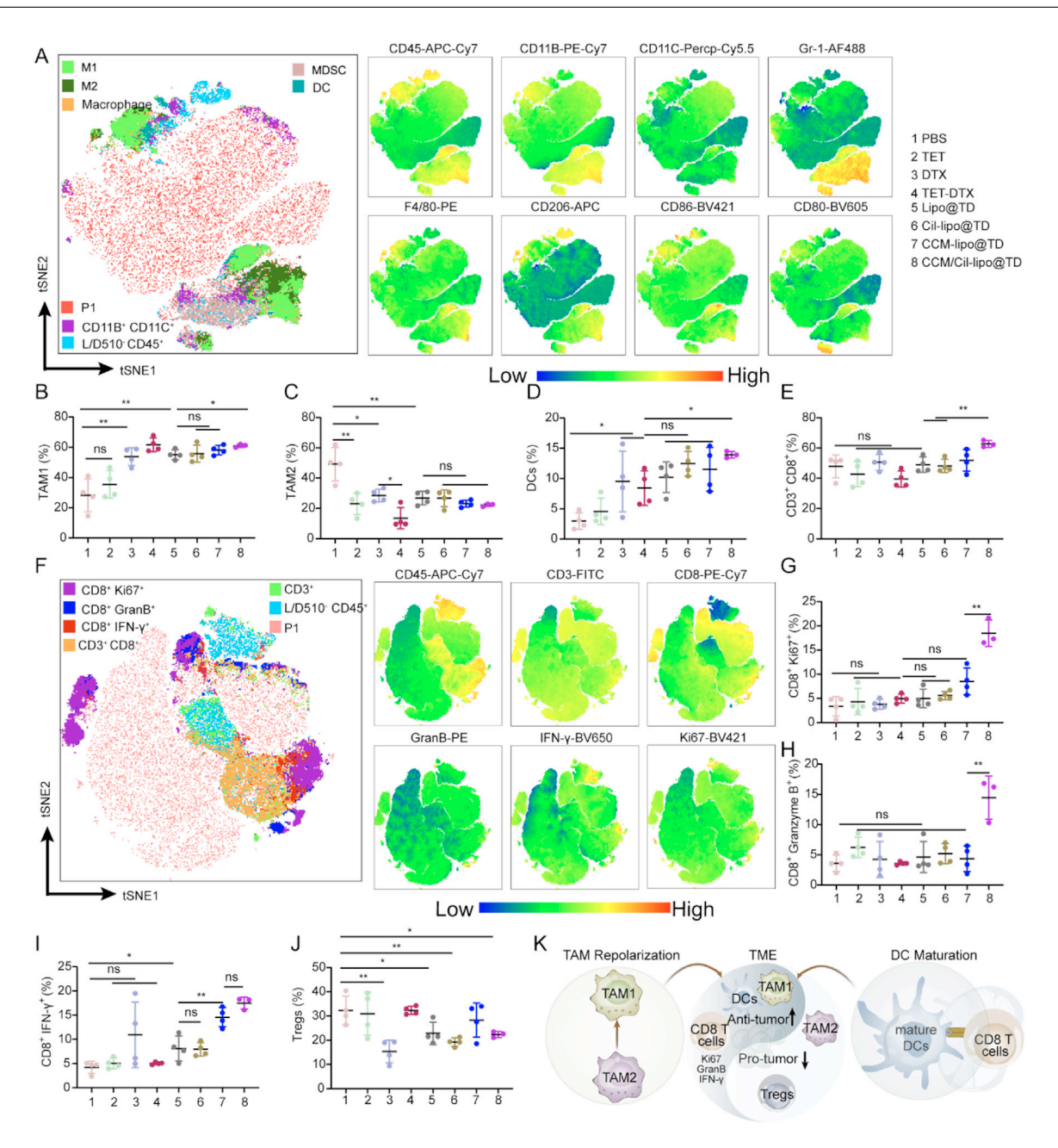


Fig. 7 – CCM/Cil-lipo@TD remodeled the immunosuppressive TME in tumor tissues. (A) t-SNE map of monocytes in tumor tissues. Cytometric analysis and quantitative analysis of (B) TAM1s (CD206^{low} CD86⁺), (C) TAM2s (CD86^{low} CD206⁺), (D) DCs (CD11B⁺ CD11C⁺ CD80⁺ CD86⁺), (E) CD3⁺ CD8⁺ T, (G) CD8⁺ Ki67⁺ T, (H) CD8⁺ Granzyme B⁺ T, (I) CD8⁺ IFN- γ ⁺ T, and (J) Tregs (CD25⁺ Foxp3⁺). (n = 3 of CCM/Cil-lipo@TD group, n = 4 in the other groups). (F) t-SNE map of the intratumoral infiltration of T lymphocytes. (K) Schematic illustration of anti-tumor immune activation induced by CCM/Cil-lipo@DiD in tumor tissues. *P < 0.05, **P < 0.01.

Notably, TAM2 is correlated with poor prognosis in TNBC patients and induces the formation of an immunosuppressive TME [50]. The TCGA database revealed significant macrophage infiltration in breast-invasive carcinoma patients (https://tcia.at/cellTypeFractions) (Fig. S7B). Moreover, M1 macrophages were significantly associated with improved overall survival (HR=0.815, p=0.0083), whereas M2 macrophages were associated with much worse prognoses (HR=1.32, p=0.000349), suggesting that TNBC

survival is associated with macrophage polarization (Fig. S7C and S7D). To further investigate the TME immunomodulatory effect of CCM/Cil-lipo@TD, the repolarization of TAMs in tumor tissues was examined. Immunofluorescence imaging demonstrated that CCM/Cil-lipo@TD efficiently repolarized TAM2 toward TAM1 (Fig. S8A–S8C). The t-stochastic neighbor embedding (t-SNE) method was utilized for the visualization of monocyte activation in tumor tissues, where the individual cell types were colored with graph-based clustering (Fig. 7A).

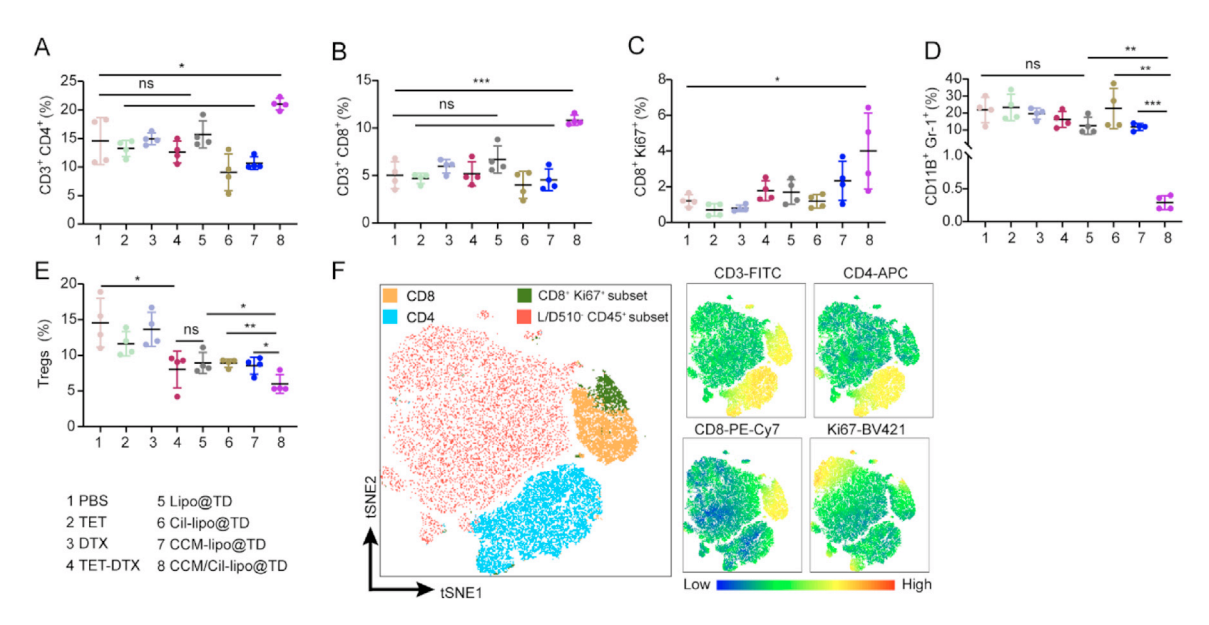


Fig. 8 – CCM/Cil-lipo@TD remodeled the immune microenvironment in the spleen. Cytometric analysis and quantitative analysis of (A) CD3⁺ CD4⁺ T, (B) CD3⁺ CD8⁺ T, (C) CD8⁺ Ki67⁺ T, (D) MDSCs (CD11B⁺ Gr-1⁺), and (E) Tregs (CD25⁺ Foxp3⁺) (n = 4); (F) t-SNE map of T lymphocytes in the spleen. *P < 0.05, **P < 0.01, ***P < 0.001.

Flow cytometry results further demonstrated increased TAM1 and decreased TAM2 populations after CCM/Cil-lipo@TD treatment (Fig. 7B, C and S9A, S9B). These findings suggest that CCM/Cil-lipo@TD effectively inhibited SOS1 expression and inactivated Akt and ERK signaling, thereby promoting TAM reprogramming.

Furthermore, TAM2 infiltration within tumor tissues can inhibit DC maturation [51]. As specialized antigen-presenting cells, DCs are regarded as the key to activating T cellinduced immunity. However, the immunosuppressive TME of TNBC also causes the immaturity of DCs [52]. Moreover, lowdose DTX-triggered ICD in tumor cells enhances antitumor immunity. Immunofluorescence analysis confirmed that CRT expression in the CCM/Cil-lipo@TD group was 2.3-fold and 1.3-fold higher than that observed in the PBS and TET-DTX groups, respectively (Fig. S8A and S8C). Subsequently, DC maturation was determined via flow cytometry (Fig. 7D, S9A and S9C). The CCM/Cil-lipo@TD treatment elevated the percentage of mature DCs in the tumors, showing 4.7- and 1.7-fold higher levels than those in the PBS and TET-DTX groups, respectively (Fig. 7D). Activated DCs present antigens to naive T lymphocytes, thereby promoting antitumor Tcell responses [53]. The enhanced infiltration of TAM1s and DCs in tumor tissues might cause an improved T-cellmediated immune response (Fig. 7E-K). t-SNE was further utilized for the visualization of T-cell activation in tumor tissues, where the individual cell types were colored with graph-based clustering (Fig. 7F). The results showed that the CCM/Cil-lipo@TD treatment significantly enhanced the intratumoral infiltration of T cells (CD3+ CD8+ T), showing 1.6- and 1.3-fold higher levels than those of the TET-DTX and Lipo@TD groups, respectively (Fig. 7E, S10A and S10B). Moreover, the number of proliferative T cells (CD8⁺ Ki 67⁺) of the CCM/Cil-lipo@TD group was 3.7-, 3.3- and 2.2-fold higher levels compared with those of Lipo@TD, Cil-lipo@TD, and CCM-lipo@TD groups, respectively (Fig. 7G, S10A and S10C). Compared with the Lipo@TD group, the CCM/Cillipo@TD also significantly elevated the proportion of cytotoxic T lymphocytes (CD8⁺ IFN- γ ⁺, CD8⁺ GranzymeB⁺) (Fig. 7H, I and S11A, S11B).

In addition, TAM2 recruits Tregs, which are highly correlated with immunosuppressive functions [51]. The intratumoral infiltration of immunosuppressive Tregs in the CCM/Cil-lipo@TD group decreased by 30.8 % compared to the TET-DTX group (Fig. 7J, S12A and S12B). However, compared to DTX treatment, TET-DTX treatment had the opposite effect, possibly due to TET-induced Treg differentiation [54], which was not observed in the CCM/Cil-lipo@TD group. Collectively, these results indicated that CCM/Cil-lipo@TD could ameliorate the immunosuppressive TME to improve the anti-TNBC effects (Fig. 7K).

In addition to tumor tissue, we also observed a large amount of CCM/Cil-lipo@DiD accumulation in other secondary lymphoid organs (e.g., spleen) dominated by T cells. As shown in Fig. S6A and S6B, CCM/Cil-lipo@TD treatment normalized splenomegaly in 4T1-bearing mice. Flow cytometry analysis was further utilized to determine the phenotype and frequency of immune cells in the spleen (Fig. 8). As shown in Fig. 8A-8C and S13, compared with the PBS group, the CCM/Cil-lipo@TD group presented significantly greater proportions of CD4+ T (1.4-fold higher), CD8+ T (2.1fold higher), and CD8+ Ki67+ (3.3-fold higher) cells in the spleen after treatment, whereas no differences were observed in the other groups. Moreover, CCM/Cil-lipo@TD significantly reduced the frequency of splenic MDSCs (Fig. 8D and S14A). In addition, the splenic infiltration of immunosuppressive Tregs in the CCM/Cil-lipo@TD group was lower than that observed in the other liposome groups (Fig.8E and S14B). The t-SNE was further utilized for the visualization of T-cell activation in the spleen, where the individual cell types were colored

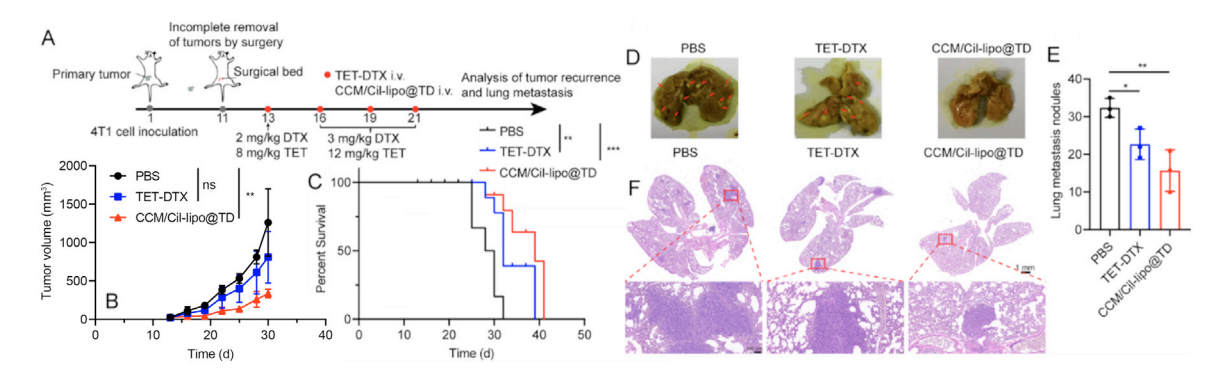


Fig. 9 – CCM/Cil-lipo@TD inhibited postsurgery recurrence of 4T1 tumors in vivo. (A) Schematic of the treatment schedule in a recurrence 4T1 mouse model; (B) Tumor growth curve during the TET-DTX and CCM/Cil-lipo@TD treatment (n = 3); (C) Survival curve of recurrent 4T1 mice after treatment (n = 6); (D) Lung photographs and (E) quantitative results of metastatic nodules from the mice after treatment (n = 3); (F) H&E-stained lung slices after TET-DTX and CCM/Cil-lipo@TD treatment. Scale bar: 1 mm & 100 μ m. *P < 0.05, **P < 0.01, ***P < 0.001.

with graph-based clustering (Fig. 8F). These data indicated that CCM/Cil-lipo@TD induced effective systemic antitumor immune responses in the spleen with increased functions of CD4 $^+$ T cells and CD8 $^+$ T cells, as well as a reduced frequency of Tregs and MDSCs.

Collectively, these findings demonstrated that CCM/Cillipo@TD induced strong tumor immune and systemic immune responses via the synergistic effects of SOS1 inhibition, low-dose DTX-induced ICD, and tumor hypoxia alleviation.

3.10. CCM/Cil-lipo@TD inhibited post-surgery recurrence of 4T1 tumors

After confirming the TME reshaping capacity of CCM/Cillipo@TD, we further investigated the effect of CCM/Cillipo@TD on TNBC recurrence. A 4T1 partial tumor resection model was established to simulate postoperative TNBC recurrence (Fig. 9A). The mice were treated with TET-DTX and CCM/Cil-lipo@TD (equivalent to the dosage of TET-DTX), immediately after surgery on Day 13. The TET-DTX combination had limited therapeutic effects on tumor growth; in contrast, CCM/Cil-lipo@TD significantly delayed the growth of recurrent tumors (Fig. 9B). In this case, the median survival of the CCM/Cil-lipo@TD group improved to 39 d compared with that of the TET-DTX group (32 d, Fig. 9C). Additionally, the CCM/Cil-lipo@TD group showed significantly fewer metastatic foci, whereas PBS and TET-DTX groups exhibited extensive metastasis (Fig. 9D-F). These results suggested that CCM/Cillipo@TD could effectively inhibit TNBC recurrence and lung metastasis.

4. Conclusions

To achieve specific tumor targeting and effective deep intratumoral drug delivery, we developed a biomimetic liposome platform (CCM/Cil-lipo@TD) that co-delivers TET and DTX. CCM/Cil-lipo@TD demonstrated preferential accumulation in breast tumors and permeated deeply into

tumor tissues; this locally released TET repolarized TAM2 toward TAM1 via SOS1 inhibition, while low-dose DTX induced DC maturation via ICD stimulation. Furthermore, the CCM/Cil-lipo@TD alleviated tumor hypoxia via HIF-1 α inhibition. Taken together, CCM/Cil-lipo@TD exhibited a synergistic advantage in terms of these immune activating functions, thus relieving the suppressive TME. While TAM reprogramming has been widely studied in TNBC, our work demonstrates selective modulation of macrophage polarization by targeted inhibition of SOS1 on tumor cells. Together with this indirect TAM regulation and low-dose DTX-induced ICD of tumor cells, CCM/Cil-lipo@TD exerted superior tumor inhibition (82.9 %) in 4T1 orthotopic models. We further confirmed CCM/Cil-lipo@TD as a promising nanovehicle with enhanced tumor suppression capacity which also circumvents the high dose toxicity of DTX in TNBC. In addition, CCM/Cil-lipo@TD significantly prolonged overall survival by inhibiting postoperative local recurrence and distant metastasis. Taken together, the Cil-engineered breast CCM-fused biomimetic liposome system is highly promising for TNBC immunotherapy. Despite these advances, there are still some limitations. First, systematic screening of alternative SOS1 could optimize therapeutic synergy. Second, much work is still necessary to determine the mechanism by which TET regulates SOS1. Third, clinical translation still faces challenges. One of the cost-related challenges is to obtain and store material from type-matched donors [41]. Importantly, biomimetic cell membranes are classified as biologics, which require new assays to meet the quality standards for clinical applications, including potential immunogenic responses and long-term effects [55]. The other challenge is the scale-up and manufacturing of stable CCM-based biomimetic vehicles. The characteristics of infinite proliferation incubate the potential of large-scale culture and production of CCMs in vitro [56].

Conflicts of interest

The authors declare no conflict of interest.

Acknowledgments

We thank the staff members of the Large-scale Protein Preparation System at the National Facility for Protein Science in Shanghai (NFPS), Shanghai Advanced Research Institute, Chinese Academy of Science, China for providing the Electron Microscopy System technical support and assistance in data collection and analysis. This work was funded by "Shuguang Program" supported by Shanghai Education Development Foundation and Shanghai Municipal Education Commission (22SG41), and the combination of the medical care and health project of the Shanghai University of Traditional Chinese Medicine (YYKC-2021–01–008).

Supplementary materials

Supplementary material associated with this article can be found, in the online version, at doi:10.1016/j.ajps.2025.101064. The figures and tables with "S" before the serial number are included in the Supplementary material.

REFERENCES

- [1] Derakhshan F, Reis-Filho JS. Pathogenesis of triple-negative breast cancer. Annu Rev Pathol 2022;17:181–204.
- [2] Ding Y, Chen X, Liu C, Ge W, Wang Q, Hao X, et al. Identification of a small molecule as inducer of ferroptosis and apoptosis through ubiquitination of GPX4 in triple negative breast cancer cells. J Hematol Oncol 2021;14(1):19.
- [3] Li Y, Zhang H, Merkher Y, Chen L, Liu N, Leonov S, et al. Recent advances in therapeutic strategies for triple-negative breast cancer. J Hematol Oncol 2022;15(1):121.
- [4] Hallett RM, Dvorkin-Gheva A, Bane A, Hassell JA. A gene signature for predicting outcome in patients with basal-like breast cancer. Sci Rep 2012;2:227.
- [5] Bianchini G, De Angelis C, Licata L, Gianni L. Treatment landscape of triple-negative breast cancer - expanded options, evolving needs. Nat Rev Clin Oncol 2022;19(2):91–113.
- [6] Schmid P, Cortes J, Dent R, Pusztai L, McArthur H, Kümmel S, et al. VP7-2021: KEYNOTE-522: Phase III study of neoadjuvant pembrolizumab + chemotherapy vs. placebo + chemotherapy, followed by adjuvant pembroli zumab vs. placebo for early-stage TNBC. Ann Oncol 2021;32(9):1198-200.
- [7] Liu Y, Hu Y, Xue J, Li J, Yi J, Bu J, et al. Advances in immunotherapy for triple-negative breast cancer. Mol Cancer 2023;22(1):145.
- [8] Harris MA, Savas P, Virassamy B, O'Malley MMR, Kay J, Mueller SN, et al. Towards targeting the breast cancer immune microenvironment. Nat Rev Cancer 2024;24(8):554–77.
- [9] Mehta AK, Cheney EM, Hartl CA, Pantelidou C, Oliwa M, Castrillon JA, et al. Targeting immunosuppressive macrophages overcomes PARP inhibitor resistance in BRCA1-associated triple-negative breast cancer. Nat Cancer 2021;2(1):66–82.
- [10] Mantovani A, Allavena P, Marchesi F, Garlanda C. Macrophages as tools and targets in cancer therapy. Nat Rev Drug Discov 2022;21(11):799–820.
- [11] Zou S, Tong Q, Liu B, Huang W, Tian Y, Fu X. Targeting STAT3 in cancer immunotherapy. Mol Cancer 2020;19(1): 145.

- [12] Kundu M, Butti R, Panda VK, Malhotra D, Das S, Mitra T, et al. Modulation of the tumor microenvironment and mechanism of immunotherapy-based drug resistance in breast cancer. Mol Cancer 2024;23(1):92.
- [13] Xiang X, Wang J, Lu D, Xu X. Targeting tumor-associated macrophages to synergize tumor immunotherapy. Signal Transduct Target Ther 2021;6(1):75.
- [14] Singhal A, Li BT, O'Reilly EM. Targeting KRAS in cancer. Nat. Med. 2024;30(4):969–83.
- [15] Xing F, Zhao D, Wu SY, Tyagi A, Wu K, Sharma S, et al. Epigenetic and posttranscriptional modulation of SOS1 can promote breast cancer metastasis through obesity-activated c-Met signaling in African-American women. Cancer Res 2021;81(11):3008–21.
- [16] Duan X, Chan C, Lin W. Nanoparticle-mediated immunogenic cell death enables and potentiates cancer immunotherapy. Angew Chem Int Ed Engl 2019;58(3):670–80.
- [17] Zhang L, Zhou Y, Chai X, Yang Z, Pang N, Du Y, et al. Excipient-free prodrug-based three-in-one nanoparticles co-deliver diversified agents to amplify tumor therapy. Chem Engineer J 2022;435:134880.
- [18] Zhou W, Zhou Y, Chen X, Ning T, Chen H, Guo Q, et al. Pancreatic cancer-targeting exosomes for enhancing immunotherapy and reprogramming tumor microenvironment. Biomaterials 2021;268:120546.
- [19] Wang C, Zhang R, He J, Yu L, Li X, Zhang J, et al. Ultrasound-responsive low-dose doxorubicin liposomes trigger mitochondrial DNA release and activate cGAS-STING-mediated antitumour immunity. Nat Commun 2023;14(1):3877.
- [20] Bhagya NC, Chandrashekar KR. Tetrandrine and cancer an overview on the molecular approach. Biomed Pharmacother 2018;97:624–32.
- [21] Jiang YW, Cheng HY, Kuo CL, Way TD, Lien JC, Chueh FS, et al. Tetrandrine inhibits human brain glioblastoma multiforme GBM 8401 cancer cell migration and invasion in vitro. Environ Toxicol 2019;34(4):364–74.
- [22] Liu T, Li K, Zhang Z, Peng J, Yang J, Law BYK, et al. Tetrandrine inhibits cancer stem cell characteristics and epithelial to mesenchymal transition in triple-negative breast cancer via SOD1/ROS signaling pathway. Am J Chin Med 2023;51(2):425–44.
- [23] Fang RH, Gao W, Zhang L. Targeting drugs to tumours using cell membrane-coated nanoparticles. Nat Rev Clin Oncol 2023;20(1):33–48.
- [24] Nie D, Dai Z, Li J, Yang Y, Xi Z, Wang J, et al. Cancer-cell-membrane-coated nanoparticles with a yolk-shell structure augment cancer chemotherapy. Nano Lett 2020;20(2):936–46.
- [25] Wong PP, Demircioglu F, Ghazaly E, Alrawashdeh W, Stratford MR, Scudamore CL, et al. Dual-action combination therapy enhances angiogenesis while reducing tumor growth and spread. Cancer Cell 2015;27(1):123–37.
- [26] Zhao X, Ni S, Song Y, Hu K. Intranasal delivery of Borneol/R8dGR peptide modified PLGA nanoparticles co-loaded with curcumin and cisplatin alleviate hypoxia in pediatric brainstem glioma which improves the synergistic therapy. J Control Release 2023;362:121–37.
- [27] Zhao C, Shao L, Lu J, Deng X, Tong Y, Wu Y. Hybrid prodrug nanoparticles with tumor penetration and programmed drug activation for enhanced chemoresistant cancer therapy. ACS Appl Mater Interfaces 2017;9(22):18450–61.
- [28] Li X, Yu N, Li J, Bai J, Ding D, Tang Q, et al. Novel "Carrier-free" nanofiber codelivery systems with the synergistic antitumor effect of paclitaxel and tetrandrine through the enhancement of mitochondrial apoptosis. ACS Appl Mater Interfaces 2020;12(9):10096–106.
- [29] Sharma P, Stecklein SR, Yoder R, Staley JM, Schwensen K, O'Dea A, et al. Clinical and biomarker findings of neoadjuvant

- pembrolizumab and carboplatin plus docetaxel in triple-negative breast cancer: neoPACT Phase 2 clinical trial. JAMA Oncol 2024;10(2):227–35.
- [30] Zhang Y, Chen X, Yuan Q, Bian Y, Li M, Wang Y, et al. Enzyme-activated near-infrared fluorogenic probe with high-efficiency intrahepatic targeting ability for visualization of drug-induced liver injury. Chem Sci 2021;12(44):14855–62.
- [31] Wu T, Hou X, Li J, Ruan H, Pei L, Guo T, et al. Microneedle-mediated biomimetic cyclodextrin metal organic frameworks for active targeting and treatment of hypertrophic scars. ACS Nano 2021;15(12):20087–104.
- [32] Kong H, Zheng C, Yi K, Mintz RL, Lao YH, Tao Y, et al. An antifouling membrane-fusogenic liposome for effective intracellular delivery in vivo. Nat Commun 2024;15(1):4267.
- [33] Hariharan S, Gustafson D, Holden S, McConkey D, Davis D, Morrow M, et al. Assessment of the biological and pharmacological effects of the alpha nu beta3 and alpha nu beta5 integrin receptor antagonist, cilengitide (EMD 121974), in patients with advanced solid tumors. Ann Oncol 2007;18(8):1400–7.
- [34] Reynolds AR, Hart IR, Watson AR, Welti JC, Silva RG, Robinson SD, et al. Stimulation of tumor growth and angiogenesis by low concentrations of RGD-mimetic integrin inhibitors. Nat Med 2009;15(4):392–400.
- [35] Li J, Wang H, Wang Y, Gong X, Xu X, Sha X, et al. Tumor-activated size-enlargeable bioinspired lipoproteins access cancer cells in tumor to elicit anti-tumor immune responses. Adv Mater 2020;32(38):e2002380.
- [36] Guo J, Zou Y, Huang L. Nano delivery of chemotherapeutic ICD inducers for tumor immunotherapy. Small Meth 2023;7(5):e2201307.
- [37] Chen Q, Zhang L, Li L, Tan M, Liu W, Liu S, et al. Cancer cell membrane-coated nanoparticles for bimodal imaging-guided photothermal therapy and docetaxel-enhanced immunotherapy against cancer. J Nanobiotechnol 2021;19(1):449.
- [38] Eisenbarth SC. Dendritic cell subsets in T cell programming: location dictates function. Nat Rev Immunol 2019;19(2):89–103.
- [39] Vitale I, Manic G, Coussens LM, Kroemer G, Galluzzi L. Macrophages and metabolism in the tumor microenvironment. Cell Metab 2019;30(1):36–50.
- [40] Wang H, Tang Y, Fang Y, Zhang M, Wang H, He Z, et al. Reprogramming tumor immune microenvironment (TIME) and metabolism via biomimetic targeting codelivery of Shikonin/JQ1. Nano Lett 2019;19(5):2935–44.
- [41] Fang RH, Kroll AV, Gao W, Zhang L. Cell membrane coating nanotechnology. Adv Mater 2018;30(23):e1706759.
- [42] Kim HY, Kang M, Choo YW, Go SH, Kwon SP, Song SY, et al. Immunomodulatory lipocomplex functionalized with photosensitizer-embedded cancer cell membrane inhibits tumor growth and metastasis. Nano Lett 2019;19(8):5185–93.
- [43] Fang H, Gai Y, Wang S, Liu Q, Zhang X, Ye M, et al. Biomimetic oxygen delivery nanoparticles for enhancing photodynamic

- therapy in triple-negative breast cancer. J Nanobiotechnol 2021;19(1):81.
- [44] Wang W, Zhang X, Li Z, Pan D, Zhu H, Gu Z, et al. Dendronized hyaluronic acid-docetaxel conjugate as a stimuli-responsive nano-agent for breast cancer therapy. Carbohydr Polym 2021;267:118160.
- [45] Zhao Y, Zheng Y, Zhu Y, Li H, Zhu H, Liu T. Docetaxel-loaded M1 macrophage-derived exosomes for a safe and efficient chemoimmunotherapy of breast cancer. J Nanobiotechnol 2022;20(1):359.
- [46] Ju C, Zhou M, Du D, Wang C, Yao J, Li H, et al. EIF4A3-mediated circ_0042881 activates the RAS pathway via miR-217/SOS1 axis to facilitate breast cancer progression. Cell Death Dis 2023;14(8):559.
- [47] Hofmann MH, Gmachl M, Ramharter J, Savarese F, Gerlach D, Marszalek JR, et al. BI-3406, a potent and selective SOS1-KRAS interaction inhibitor, is effective in KRAS-driven cancers through combined MEK inhibition. Cancer Discov 2021;11(1):142–57.
- [48] Marasco M, Kumar D, Seale T, Borrego SG, Kaplun E, Aricescu I, et al. Concurrent SOS1 and MEK suppression inhibits signaling and growth of NF1-null melanoma. Cell Rep Med 2024;5(11):101818.
- [49] Chu X, Tian Y, Lv C. Decoding the spatiotemporal heterogeneity of tumor-associated macrophages. Mol Cancer 2024;23(1):150.
- [50] Weng YS, Tseng HY, Chen YA, Shen PC, Al Haq AT, Chen LM, et al. MCT-1/miR-34a/IL-6/IL-6R signaling axis promotes EMT progression, cancer stemness and M2 macrophage polarization in triple-negative breast cancer. Mol Cancer 2019;18(1):42.
- [51] Mantovani A, Marchesi F, Malesci A, Laghi L, Allavena P. Tumour-associated macrophages as treatment targets in oncology. Nat Rev Clin Oncol 2017;14(7):399–416.
- [52] Huang S, Wen T, Wang J, Wei H, Xiao Z, Li B, et al. Nanoparticle-integrated dissolving microneedles for the co-delivery of R848/aPD-1 to synergistically reverse the immunosuppressive microenvironment of triple-negative breast cancer. Acta Biomater 2024;176:344–55.
- [53] Del Prete A, Salvi V, Soriani A, Laffranchi M, Sozio F, Bosisio D, et al. Dendritic cell subsets in cancer immunity and tumor antigen sensing. Cell Mol Immunol 2023;20(5):432–47.
- [54] Fang Y, Zhang Q, Yuan X, Lv C, Zhang J, Zhu Y, et al. Tetrandrine, an immunosuppressive alkaloid isolated from Steohania tetrandra S. Moore, induces the generation of treg cells through enhancing fatty acid oxidation. Immunology 2022;166(4):492–506.
- [55] Ma Y, Yi J, Ruan J, Ma J, Yang Q, Zhang K, et al. Engineered cell membrane-coated nanoparticles: new strategies in glioma targeted therapy and immune modulation. Adv Healthc Mater 2024;13(20):e2400514.
- [56] Li S, Meng X, Peng B, Huang J, Liu J, Xiao H, et al. Cell membrane-based biomimetic technology for cancer phototherapy: mechanisms, recent advances and perspectives. Acta Biomater 2024;174:26–48.